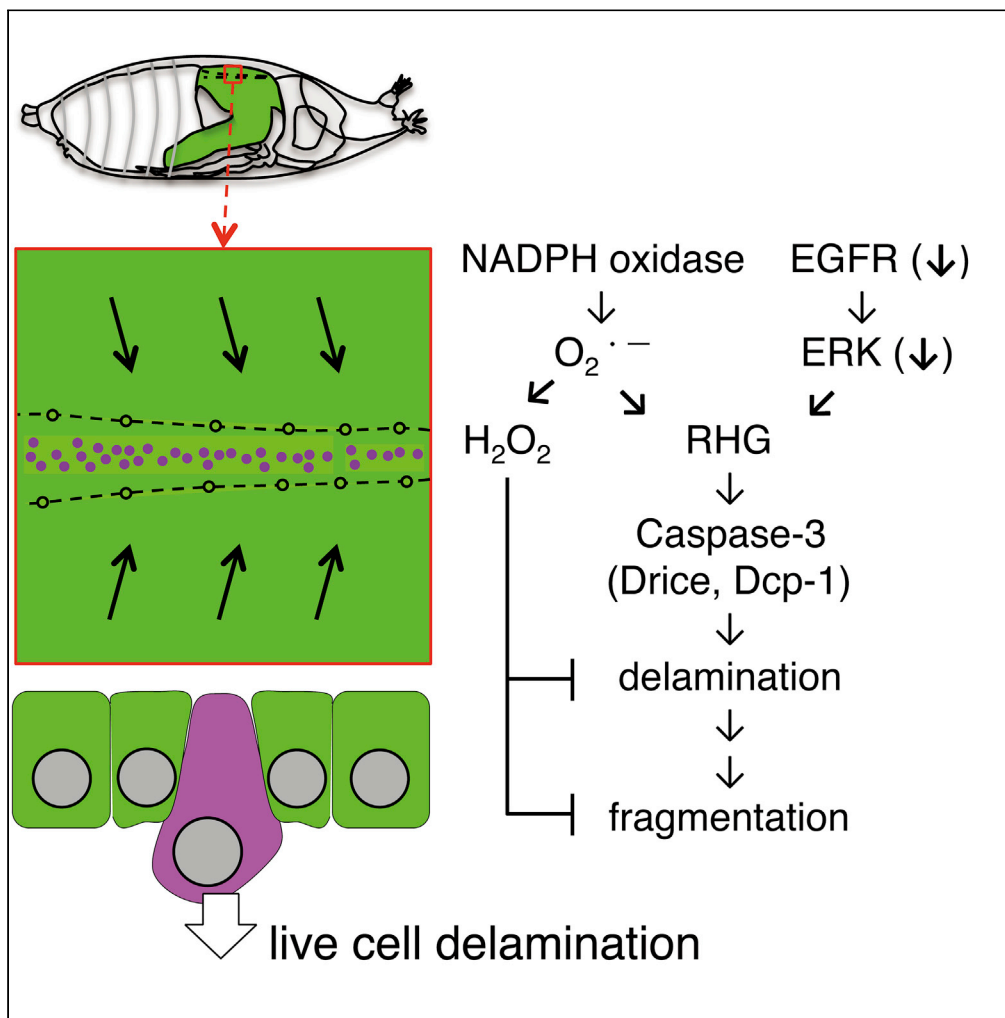**Article**

ROS Regulate Caspase-Dependent Cell Delamination without Apoptosis in the *Drosophila* Pupal Notum

Yuya Fujisawa,
Natsuki Shinoda,
Takahiro Chihara,
Masayuki Miura

miura@mol.f.u-tokyo.ac.jp

HIGHLIGHTS

NADPH oxidases are responsible for cell delamination in *Drosophila* pupal notum

Nox is upregulated in delaminating cells prior to caspase-3 activation

Nox promotes caspase-3 activation and cell delamination

H_2O_2 suppresses apoptotic nuclear fragmentation during delamination

iScience

Article

ROS Regulate Caspase-Dependent Cell Delamination without Apoptosis in the *Drosophila* Pupal Notum

Yuya Fujisawa,[1] Natsuki Shinoda,[1] Takahiro Chihara,[2,3] and Masayuki Miura[1,4,*]

SUMMARY

Thorax fusion occurs in the midline of the *Drosophila* pupal notum and involves epithelial cell delamination requiring apoptotic signaling. By genetic screening, we found that NADPH oxidases (Nox and Duox) associated with superoxide anion (O^-_2) are responsible for caspase-3 activation and delamination. We observed that Nox is upregulated in cells that undergo delamination and that delamination depends on caspase activation. However, the cell morphology and the almost complete lack of propidium iodide incorporation suggested little membrane disruption and signified apoptotic modulation. These results demonstrate that most delaminating cells undergo caspase activation, but this activation is not sufficient for apoptosis. We showed that the expression of *Catalase*, encoding an H_2O_2 scavenger in the cytosol, increases delamination and induces apoptotic nuclear fragmentation in caspase-3-activated cells. These findings suggest that the roles of O^-_2 and intracellular H_2O_2 for delamination differs before and after caspase-3 activation, which involves live cell delamination.

INTRODUCTION

For organ morphogenesis, two distant tissues approach and combine to form one continuous structure. Various organs such as the palate, neural tube, heart, eyes, face, and body wall are developed by this process of "tissue fusion" (Ray and Niswander, 2012). A characteristic feature of tissue fusion is the appearance of many apoptotic cells near the fusion sites. However, the regulatory mechanisms and functions of apoptosis in this context remain to be elucidated (Cuervo and Covarrubias, 2004; Cuervo et al., 2002; Farbman, 1968; Hinrichsen, 1985; Martinez-Alvarez et al., 2000; Mori et al., 1994; Yamaguchi et al., 2011).

Drosophila melanogaster thorax fusion is a remarkable model for epithelial tissue fusion (Martin-Blanco and Knust, 2001; Martin-Blanco et al., 2000). We have previously shown that sub-lethal caspase activation regulates the speed of thorax closure (Fujisawa et al., 2019). Following thorax fusion in the midline, a monolayered epithelium called the pupal notum is formed. Epithelial cells along the fusion site of the midline frequently undergo basal extrusion (delamination, Koto et al., 2011; Figure 1A). The delamination rate escalates with increasing cell size via *P110* overexpression and diminishes with decreasing cell size via *Tsc1/2* overexpression (Marinari et al., 2012). This suggests that delamination is correlated with the local crowding status of the epithelium. Furthermore, upon laser wounding, the calculation of cell movement and direction via particle image velocimetry has demonstrated that delamination is caused by mechanical compaction of the midline cells (Levayer et al., 2016). This delamination is therefore designated "crowding-induced cell delamination." Only approximately 30% of delamination is reported to be caspase dependent (Marinari et al., 2012). However, this caspase-dependent fraction has been found to be an underestimation (Levayer et al., 2016). Levayer et al. showed that major stress-sensitive pathways including p53, JNK, or Hippo Yap/Taz signaling are not involved in the delamination process (Levayer et al., 2016). The same group demonstrated that cell delamination is coupled with ERK downregulation and pro-apoptotic gene *Hid* upregulation (Moreno et al., 2019). Although ERK inactivation is limited to approximately 60% of delaminating cells with caspase-3 activation, other pathways involved in cell delamination have not yet been identified.

NADPH oxidases are involved in the generation of reactive oxygen species (ROS). These can attack a large number of biomolecules and are, therefore, associated with apoptotic cell death (Redza-Dutordoir and Averill-Bates, 2016; Wang et al., 2018). For example, spatiotemporal ROS production by NADPH oxidase is critical for tapetal programmed cell death in *Arabidopsis* (Xie et al., 2014) and is

[1]Department of Genetics, Graduate School of Pharmaceutical Sciences, The University of Tokyo, Tokyo 113-0033, Japan

[2]Department of Biological Science, Graduate School of Science, Hiroshima University, Higashi-Hiroshima, Hiroshima 739-8526, Japan

[3]Program of Biomedical Science and Basic Biology, Graduate School of Integrated Sciences for Life, Hiroshima University, Higashi-Hiroshima, Hiroshima 739-8526, Japan

[4]Lead Contact

*Correspondence: miura@mol.f.u-tokyo.ac.jp

https://doi.org/10.1016/j.isci.2020.101413
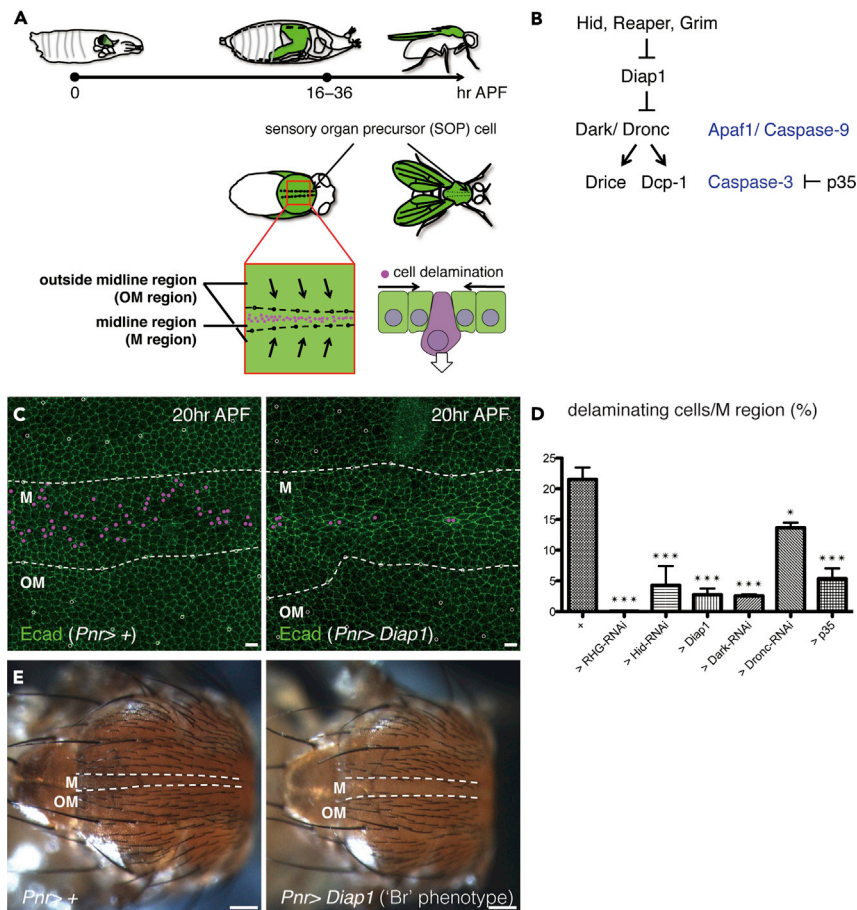
Figure 1. Apoptotic Signaling Is Required for Cell Delamination

(A) A diagram representing the development of the *Drosophila* pupal notum and the timing of cell delamination upon crowding. The boundaries between the midline (M) and outside the midline (OM) regions are outlined with dotted lines. The anterior-to-posterior axes of all pupae and adults are oriented toward the left.

(B) A diagram representing the *Drosophila* apoptotic signaling pathway.

(C) Snapshots from the movie, z-projections of confocal stacks in the pupal notum of a live fly expressing *Ecad:GFP* (20 h after puparium formation; APF). Magenta dots indicate cells that delaminated in 10 h (from 20 to 30 h APF).

(D) The ratio of cell delamination (from 20 to 30 h APF; control: four nota, versus *RHG-RNAi*, *Hid-RNAi*, *Diap1*, *Dark-RNAi*, *Dronc-RNAi*, or *p35*: three nota under the control of *Pnr-Gal4*). The p value was calculated by one-way analysis of variance (ANOVA) with Dunnett's test. *, $p < 0.05$ and ***, $p < 0.005$. Error bars indicate standard error of the mean.

(E) Images of the adult notum. Compared with the control, tissues with overexpressed *Diap1* showed a "broaden (Br) phenotype" of the M region.

The boundaries between the M and OM regions are outlined with dotted white lines. The anterior-to-posterior axes of all pupae and adults are oriented toward the left. Scale bars: (C) 10 and (E) 100 μm.

See also Figure S1.

essential for follicle cell rupture during *Drosophila* ovulation (Li et al., 2018). Most studies exploring the involvement of NADPH oxidase in caspase activation and apoptosis are based on *in vitro* or *ex vivo* experimental models, and regulation of cellular functions by NADPH oxidases have not been specifically examined *in vivo* at the single cell level. The NADPH oxidase Nox is involved in superoxide anion (O^-_2) production.

In this study, we found, by genetic screening, that Nox regulates caspase-3 activation and delamination, independent of ERK downregulation. Furthermore, we showed that intracellular hydrogen peroxide (H_2O_2) enables cells to undergo delamination without apoptotic features downstream of caspase-3 activation. ROS generated by Nox (O^-_2) and intracellular H_2O_2 can thus differentially regulate cell delamination both upstream and downstream of caspase-3 activation.

CellPress
OPEN ACCESS

RESULTS

Genetic Screen for Cell Delamination

There are differing opinions regarding the requirement of caspase activation for crowding-induced cell delamination (Levayer et al., 2016; Marinari et al., 2012). We therefore tested whether apoptotic signaling is required for delamination (Figure 1B). Overexpressing *Diap1* was sufficient to suppress the delamination rate in the midline region, which has been previously defined (M region; Figures 1C and 1D) (Levayer et al., 2016). In addition, the delamination rate was significantly reduced when *Reaper*, *Hid*, and *Grim* (*RHG*, three antagonists for an endogenous caspase inhibitor Diap1)-*RNAi*, *Dark-RNAi*, *Dronc-RNAi*, or *p35* was expressed (Figure 1D). This confirmed that apoptotic signaling is necessary for delamination. Flies that overexpressed *Diap1* showed a "broaden (Br) phenotype" on the adult notum (Figure 1E). This is consistent with a previous report, wherein the absence of caspase activation-induced delamination increased the final size of the M region (Levayer et al., 2016). Using this phenotype as an indicator for the lack of cell delamination, we sought to identify the molecules involved in cell delamination.

To this end, we conducted a genetic screen using *Pnr-Gal4* as a control (Figure S1A). We crossed overexpression or inhibition lines based on genes selected from cellular functions such as cell death, mechano-sensing, cytoskeleton formation, and oxidative stress. As shown by "Br" in the first screening (Figures S1A and S1B), we found that some manipulations led to a Br phenotype. Among the first candidates, we found that the manipulation of apoptotic genes, ROS-related genes, *Foxo-RNAi*, and *Atf3* led to a Br phenotype. None of the mechano-sensing genes were picked up in the first screening, suggesting differing mechanisms of cell delamination between *Drosophila* pupal notum and other models of live-cell delamination reported in vertebrates (Eisenhoffer et al., 2012). To test whether these phenotypes could be attributed to the suppression of delamination, we performed live imaging on the pupal notum. We identified that overexpression of *Atf3*, *Sod1*, or *Sod2* or knockdown of *Foxo*, *Nox*, or *Duox* suppressed delamination. In contrast, *Catalase* or *Keap1* overexpression and *Hayan-RNAi* did not suppress delamination. Although further analyses are required for each gene manipulation, given that Br phenotype is an integrated phenotype of both cell delamination and cell proliferation, these manipulations could enhance cell proliferation (which was not assessed in the screening). It is also possible that enhancement of cell death in the M region affects the crowding status and balance of cell proliferation. Cell elimination could therefore lead to a shift to the Br phenotype. *Catalase* overexpression is examined in detail below.

NADPH Oxidases Are Responsible for Cell Delamination and Caspase-3 Activation

Among the selected genes, we focused on the suppressive effect of *Nox* or *Duox* knockdown. Both genes belong to the NADPH oxidase family and are the only two members present in *Drosophila*. NADPH oxidases have an NADPH-binding domain close to the C terminal, transfer an electron from NADPH to O_2, and produce O^-_2. We confirmed the involvement of NADPH oxidases in delamination using four independent *Nox-RNAi* lines or three *Duox-RNAi* lines (Figures 2A, 2B, S1C). To investigate the contribution of NADPH oxidases to caspase-3 activation, we monitored the ECFP/Venus ratio of the FRET-based caspase activity indicator SCAT3 (Takemoto et al., 2003) at 16 h after puparium formation (APF), continuing until 36 h APF (Figure 1A). This is the point at which cells begin to undergo delamination in the M region. We found that *Nox-RNAi* or *Duox-RNAi* inhibited caspase-3 activation, although these inhibitory effects were smaller than those of *Dark-RNAi* (Figures 2C and 2D). These data suggest the involvement of NADPH oxidases in caspase-3 activation, which is required for delamination in the M region, in addition to the involvement of Hid modulation via ERK downregulation (Moreno et al., 2019).

Nox Is Upregulated in Delaminating Cells

To validate the involvement of an NADPH oxidase in cell delamination, we first monitored Nox expression. This was done using a gene-trap Gal4 *{CRIMIC}Nox-Gal4*, in which the splicing acceptor, T2A, and the Gal4 sequence are inserted in-frame into the first intron of *nox* (Lee et al., 2018). As Gal4 is separated from the truncated (first exon) Nox protein after translation, this expression pattern is expected to reflect the endogenous transcription and translation patterns of the gene. Combining this construction with *G-TRACE* (Evans et al., 2009; Figure 3A), we monitored the spatiotemporal pattern of Nox expression from 13 h APF. This stage occurs approximately 3 h before the beginning of cell delamination (Figure 3B). Despite the time lag of approximately a few hours between Nox expression and Gal4/UAS-dependent labeling via fluorescence protein expression, cells marked with magenta (DsRed::nls) nuclei reflected "present" expression, whereas those with green (nuc::GFP) nuclei indicated cells that previously (potentially during larval stage) showed Nox expression (described as "past"; Figures 3A and 3B). Prior to the delamination stage (13–16 h APF; Figure 1A), GFP-expressing cells are rarely
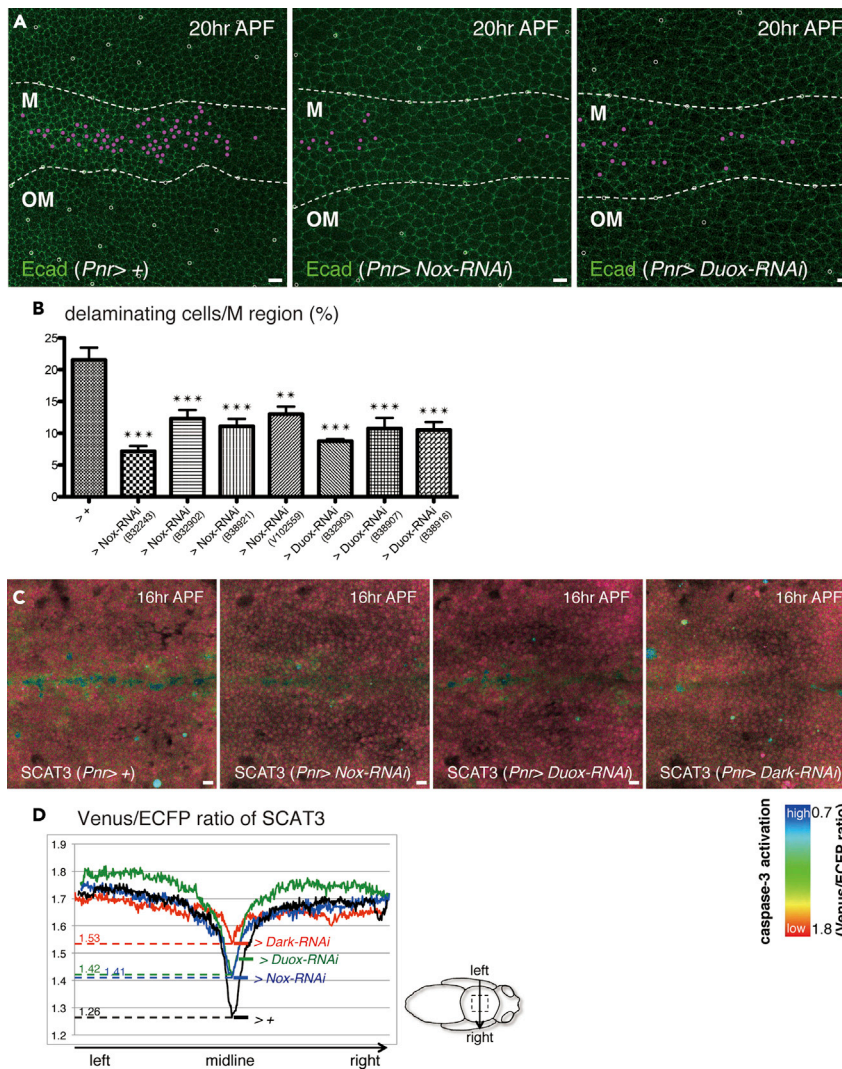
Figure 2. NADPH Oxidases Are Responsible for Cell Delamination and Caspase-3 Activation

(A) Snapshots from the movie, z-projections of confocal stacks in the pupal notum of a live fly expressing *Ecad::GFP* (20 h after puparium formation; APF). Magenta dots indicate cells that delaminated in 10 h (from 20 to 30 h APF).

(B) The ratio of cell delamination (from 20 to 30 h APF; control: four nota, versus *Nox-RNAi* or *Duox-RNAi*: three nota under the control of *Pnr-Gal4*). The p value was calculated by one-way analysis of variance (ANOVA) with Dunnett's test. **, p < 0.01 and ***, p < 0.005. Error bars indicate standard error of the mean.
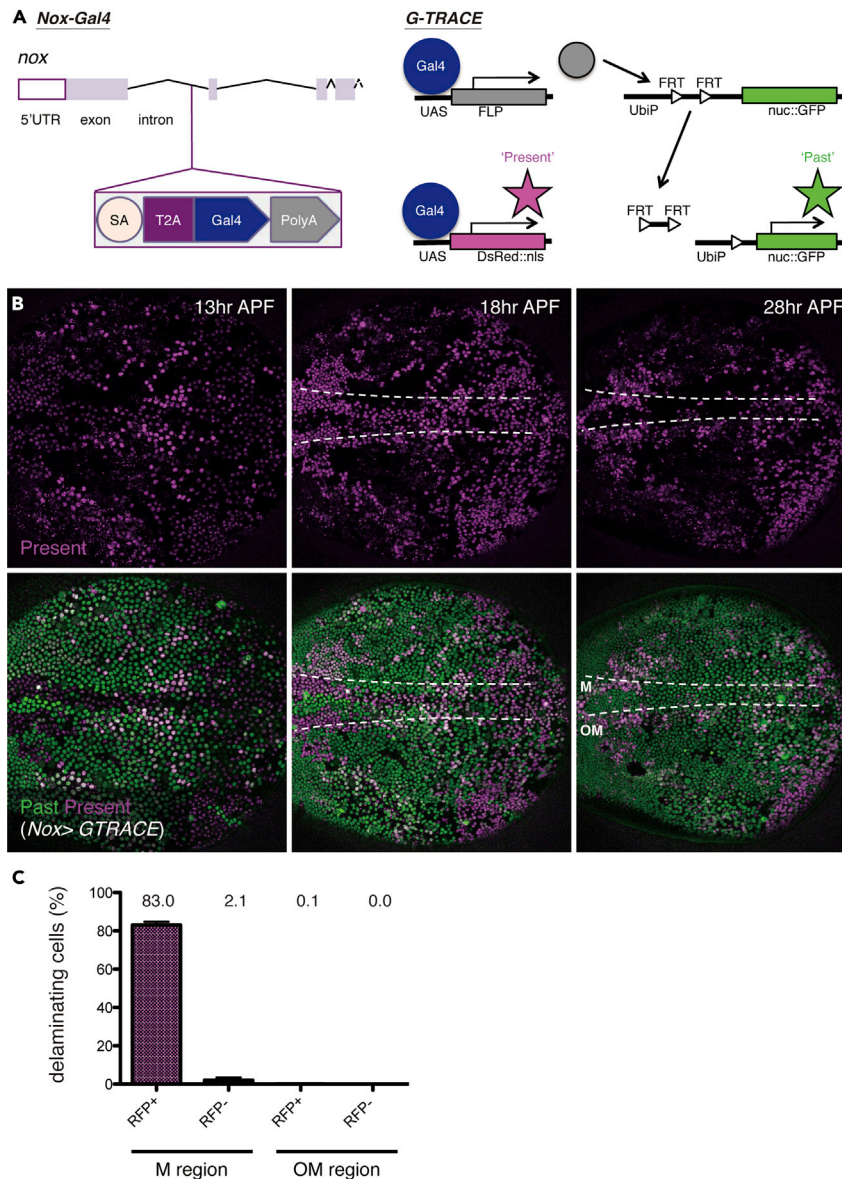
(C) Snapshots from the movie, z-projections of confocal stacks in the pupal notum of a live fly expressing SCAT3 under the control of *Pnr-Gal4* (16 h APF).

(D) Averaged changes in the FRET ratio (the Venus signal to the ECFP signal) of SCAT3 (16 h APF; control: four nota, versus *Nox-RNAi*, *Duox-RNAi*, or *Dark-RNAi*: four nota under the control of *Pnr-Gal4*).

The boundaries between the midline (M) and outside the midline (OM) regions are outlined with dotted white lines. The anterior-to-posterior axes of all pupae are oriented toward the left. Scale bars: 10 μm.

See also Figure S2.

observed in the thorax fusion site of the M region. DsRed expression instead gradually became stronger in a subset of cells at specific locations, including the M region. Such DsRed+ cells with "present" Nox expression frequently underwent delamination in the M region (83.0%; Figure 3C, Video S1). These observations suggest that, in this region, Nox functions in a cell-autonomous manner during delamination. At the delamination stage (after 16 h APF), Nox expression in cells of the M region was confirmed in the pupal notum of flies carrying *Nox::V5::TurboID*, in which the C terminus of Nox is fused with a promiscuous biotin ligase (TurboID, Branon et al., 2018; Figure S2A) that biotinylates neighboring proteins and can sensitively label TurboID-expressing cells

Figure 3. Nox Is Upregulated in Delaminating Cells

(A) *Nox-Gal4* locus and *G-TRACE* construction.

(B) Snapshots from the movie, z-projections of confocal stacks in the pupal notum of a live fly expressing *Nox-Gal4* and *G-TRACE* (13, 18, and 28 h after puparium formation; APF).

(C) The ratio of cell delamination (from 18 to 28 h APF; three nota, midline (M): 699 DsRed$^+$ cells and 638 DsRed$^-$ (GFP$^+$) cells, versus outside the midline (OM): 3,816 DsRed $^+$ cells and 3,866 DsRed$^-$ (GFP$^+$) cells). Error bars indicate standard error of the mean.

The boundaries between the M and OM regions are outlined with dotted white lines. The anterior-to-posterior axis of the pupa is oriented toward the left. Scale bars: 10 μm.

See also Figure S3 and Video S1.

(Figures S2B–S2C′). To examine whether *Nox-Gal4* "present" cells undergo delamination through caspase activation, we injected the pan-caspase inhibitor Z-VAD-fmk into the pupal notum and monitored the delamination process (Figures S3A and S3B). Consequently, Z-VAD-fmk treatment did not block the appearance of *Nox-Gal4* "present" cells but prevented delamination and increased the number of these cells in the M region at 28 h APF (Figure S3B). This further supports the idea that Nox functions upstream of caspase-3 activation to promote delamination.
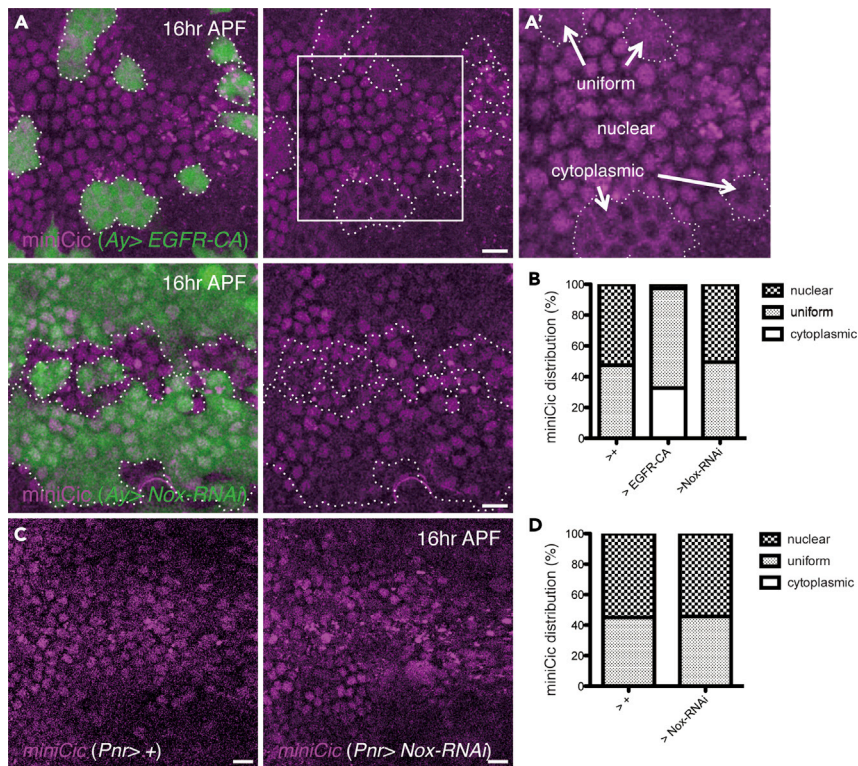
**Figure 4. Nox Is Not Involved in ERK Downregulation**

(A) Images of the z-projections of confocal stacks in the pupal notum of a live fly expressing *miniCic*, as well as green fluorescence protein (GFP) and *EGFR-CA*, under the control of *Ay-Gal4* (16 h after puparium formation; APF). (A') A magnified image of (A).

(B) Distribution of mCherry localization in the clones (16 h APF; control: three nota 222 cells, versus *EGFR-CA*: seven nota 181 cells or *Nox-RNAi*: three nota 269 cells).

(C) Images of the z-projections of confocal stacks in the pupal notum of a live fly expressing *miniCic* (16 h APF).

(D) Distribution of mCherry localization (16 h APF; control: three nota 244 cells, versus *Nox-RNAi*: three nota 188 cells). The anterior-to-posterior axes of all pupae are oriented toward the left. Scale bars: 10 μm.

Nox Is Not Involved in ERK Downregulation

A previous study showed that ERK downregulation occurs in delaminating cells (Moreno et al., 2019). This is based on the fact that the mCherry signal of the nls::C1C2Cic::mCherry (*miniCic*) reporter, which is exported from the nucleus upon phosphorylation by ERK signaling, is observed in the nucleus during delamination. This reporter reveals that, among delaminating cells, ERK downregulation occurs in approximately 60% of the caspase-3-activated cells (Moreno et al., 2019). We therefore used this reporter to determine whether Nox regulates ERK downregulation. We combined heat shock-dependent flippase expression (*Hs-flp*) and *Ay-Gal4* systems to conduct a mosaic analysis. We first expressed a constitutively active form of EGFR (*EGFR-CA*) with GFP. The mCherry signal was observed in a cytoplasmic or uniform manner in GFP$^+$ cell populations with *EGFR-CA* expression but in a nuclear or uniform manner in those without gene manipulation (control; Figures 4A and 4B). This confirmed the translocation of the *miniCic* reporter upon ERK upregulation. We detected almost no modulation of mCherry localization in GFP$^+$ cells with *Nox* knockdown compared with that in the control (Figures 4A and 4B). Consistent with this result, we found that *Nox-RNAi* via *Pnr-Gal4* did not induce mCherry cytoplasmic signals in cells around the midline (Figures 4C and 4D). These findings indicate that Nox is not responsible for ERK downregulation and that these parallel pathways regulate cell delamination in the M region of the pupal notum.

ROS Generation Is Coupled with Cell Delamination

NADPH oxidases involve ROS production. To examine the ROS levels in this tissue, we used the *in vivo* sensor for oxidative stress, *GstD-GFP* (Sykiotis and Bohmann, 2008). The GFP signal pattern indicated a high level of ROS around the midline (Figure 5A). We thus tested the correlation between ROS generation
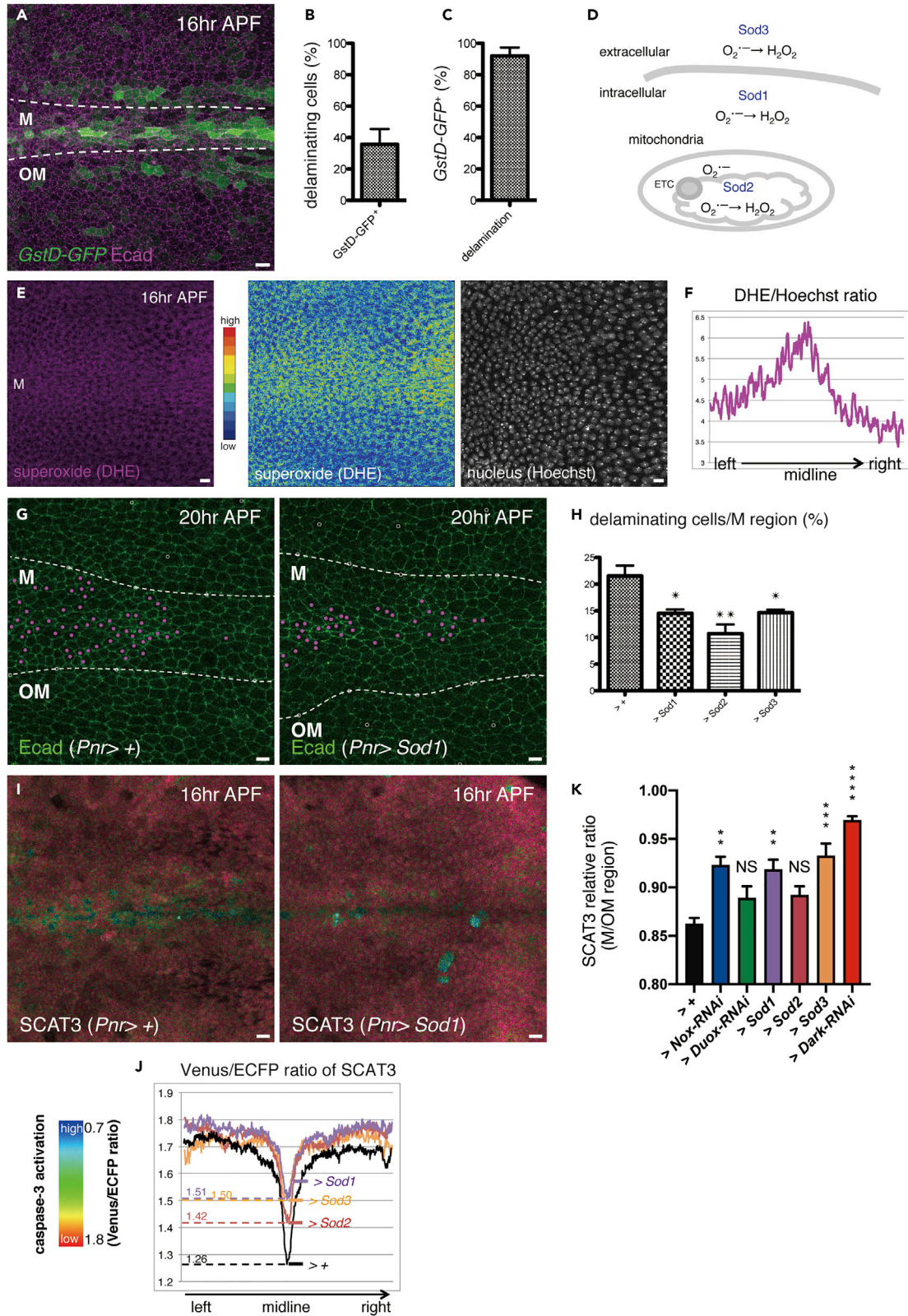
**Figure 5. Reactive Oxygen Species (ROS) Generation Is Coupled with Cell Delamination**

(A) An image of the z-projections of confocal stacks in the pupal notum of a live fly expressing *GstD-GFP* and *Ecad:tdTomato* (16 h after puparium formation; APF).

(B) The ratio of delamination in cells positive for *GstD-GFP* (from 16 to 30 h APF; three nota). Error bar indicates standard error of the mean.

(C) The ratio of *GstD-GFP*$^{+}$ cells to delaminating cells (from 16 to 30 h APF; three nota). Error bar indicates standard error of the mean.

(D) A diagram representing the conversion of produced $O^{.-}_2$ to H_2O_2 through superoxide dismutase (Sod).

(E) An image of the z-projections of confocal stacks in the pupal notum of a live fly after the injection of a mixture of DHE and Hoechst 33342.

(F) Averaged changes in the ratio of DHE signal to Hoechst 33342 signal (n = 4).

(G) Snapshots from the movie, z-projections of confocal stacks in the pupal notum of a live fly expressing *Ecad::GFP* (20 h APF). Magenta dots indicate cells that delaminated in 10 h (from 20 to 30 h APF).

(H) The ratio of cell delamination (from 20 to 30 h APF; control: four nota, versus *Sod1*, *Sod2*, or *Sod3*: three nota under the control of *Pnr-Gal4*). The p value was calculated by one-way analysis of variance (ANOVA) with Dunnett's test. *, $p < 0.05$ and **, $p < 0.01$. Error bars indicate standard error of the mean.

(I) Snapshots from the movie, z-projections of confocal stacks in the pupal notum of a live fly expressing SCAT3 under the control of *Pnr-Gal4* (16 h APF).

(J) Averaged changes in the FRET ratio (the Venus signal to the ECFP signal) of SCAT3 (16 h APF; control: four nota, versus *Sod1*: six nota, *Sod2*: five nota, or *Sod3*: four nota, under the control of *Pnr-Gal4*).

(K) Averaged changes in the FRET ratio (the Venus signal to the ECFP signal) of SCAT3 (relative values of the M region to the OM region). The p value was calculated by one-way ANOVA with Dunnett's test. NS, not significant, **, $p < 0.01$, ***, $p < 0.001$, and ****, $p < 0.0001$. Error bars indicate standard error of the mean.

The boundaries between the midline (M) and outside the midline (OM) regions are outlined with dotted white lines. The anterior-to-posterior axes of all pupae are oriented toward the left. Scale bars: 10 μm. See also Figures S4 and S5.

and cell delamination. Although only approximately 40% of the cells positive for *GstD-GFP* underwent delamination (Figure 5B), almost all delaminating cells were labeled with *GstD-GFP* (Figure 5C). As in mammals, there are three superoxide dismutases (*Sods*) present in *Drosophila*. These include *Sod1*, *Sod2*, and *Sod3*, which are involved in the conversion of intracellular, mitochondrial, and extracellular $O^{.-}_2$ to hydrogen peroxide (H_2O_2), respectively (Figure 5D). H_2O_2 oxidizes the sensor cysteine residues of Keap1, an E3-ligase of Nrf2. The oxidization of Keap1 inactivates E3-ligase activity and then Nrf2 is stabilized. Nrf2 translocates to nuclei, activates antioxidant response element, and induces the expression of genes such as *GstD* (Kansanen et al., 2013; Suzuki et al., 2019). Thus, H_2O_2 is likely to be accumulated in *GstD-GFP*-positive delaminating cells. To examine $O^{.-}_2$ production, we injected dihydroethidium (DHE) with Hoechst 33342 (Figure 5E). When normalized to that of Hoechst 33342, the DHE signal demonstrated a higher level of $O^{.-}_2$ generation in cells around the midline (Figure 5F). Besides, given that overexpressing each *Sod* solely suppressed the delamination rate (Figures 5G and 5H) and caspase-3 activation (Figures 5I and 5J), $O^{.-}_2$ reduction and an increase of H_2O_2 could suppress delamination. To further confirm the requirement of $O^{.-}_2$ production on caspase activation, we normalized the SCAT3 ratio of the M region by that of the OM region for comparison. Similar to in *Dark-RNAi*, we found that the relative ratios of SCAT3 in *Nox-RNAi*, *Sod1*, or *Sod3* were significantly increased in M region cells compared with that of the control (Figure 5K). These data suggest an involvement of $O^{.-}_2$ in caspase-3 activation around the midline.

H_2O_2 Blocks Cell Delamination after Caspase-3 Activation

H_2O_2 is known to act in redox signaling without executing cell death (Sies, 2017). Given that the expression of the $O^{.-}_2$ scavenger *Sod* promotes H_2O_2 generation, we can assume that delamination consists of the positive involvement of $O^{.-}_2$ and negative involvement of H_2O_2. Indeed, we found that the H_2O_2 scavenger *Catalase* increased delamination (Figures 6A and 6B), suggesting the inhibitory impact of H_2O_2 on delamination. We therefore wished to determine the means by which H_2O_2 suppresses caspase-mediated cell delamination.

SCAT3 monitoring revealed that *Catalase* expression did not affect caspase-3 activation (Figures S4A and S4B). Consistently, H_2O_2 and paraquat, which produce $O^{.-}_2$ and H_2O_2, similarly triggered caspase-3 activation administered to cultured S2 *Drosophila* cells (Figures S5A and S5B). These data support the notion that both $O^{.-}_2$ and H_2O_2 have the positive potential to drive caspase-3 activation. These results therefore suggest that $O^{.-}_2$ reduction by *Sods* inhibits caspase-3 activation and H_2O_2 prevents delamination after caspase-3 activation. Caspase-Tracker/CasExpress (thereafter, described as "CasT") is a Gal4-based caspase-3 activation sensor (Ding et al., 2016; Tang et al., 2015). Here, 56.4% of the CasT^{+} cells detected at 25 h APF did not undergo delamination, even after 6 h (Figures 6C–6E). We then investigated whether *CasT*-induced genetic manipulations alter the cell delamination rate by expressing *p35*, thus inhibiting the caspase activation required for delamination. As expected, *p35* expression under the control of *CasT* effectively prevented delamination (Figure 6G). Notably, *CasT*-driven *Catalase* expression significantly increased the delamination rate (Figures 6F and 6G). These findings demonstrate the inhibitory effect of H_2O_2 on cell delamination after caspase-3 activation.
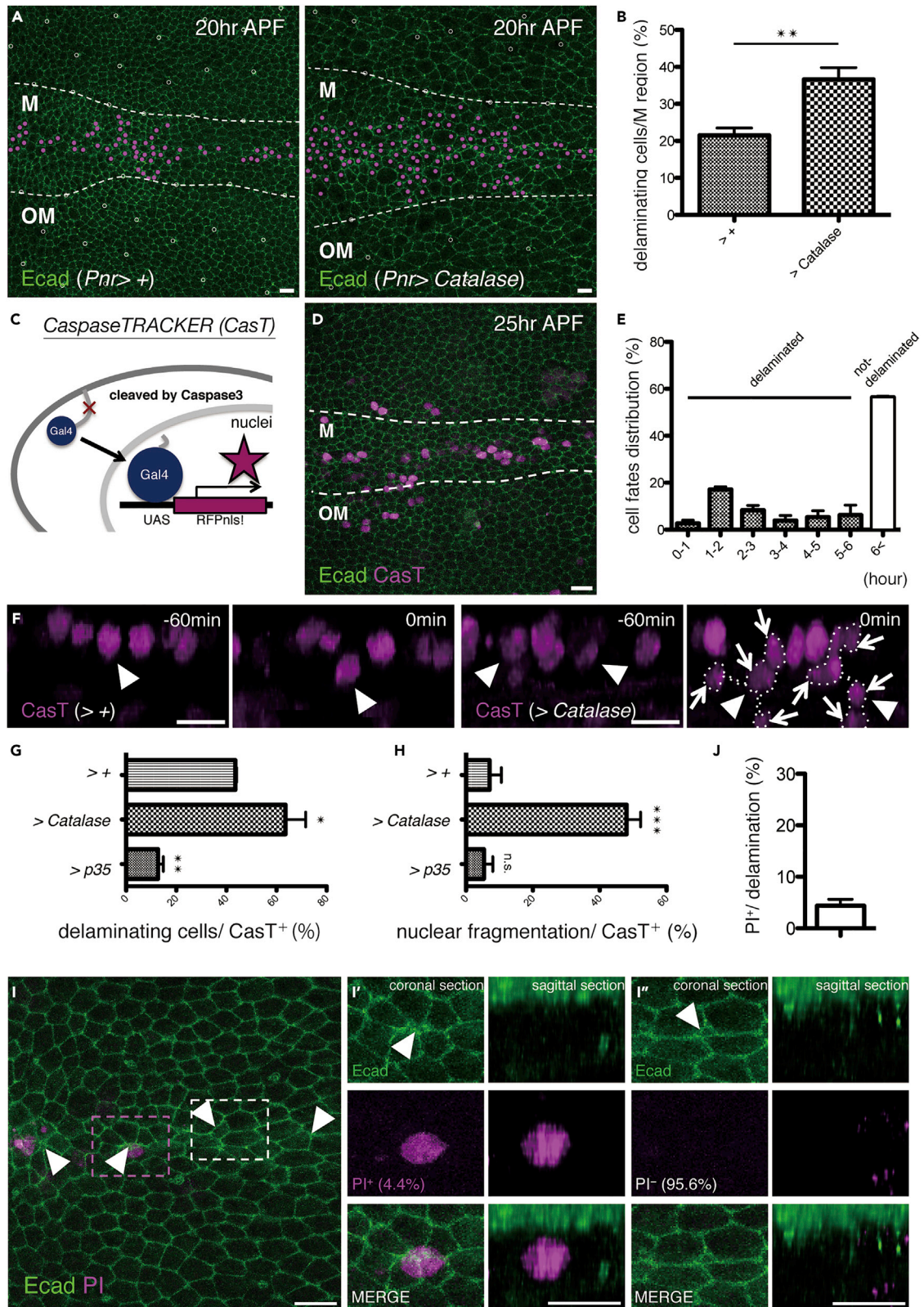
Figure 6. H$_2$O$_2$ Prevents Delaminating Cells from Apoptosis

(A) Snapshots from the movie, z-projections of confocal stacks in the pupal notum of a live fly expressing *Ecad::GFP* (20 h after puparium formation; APF). Magenta dots indicate cells that delaminated in 10 h (from 20 to 30 h APF).

(B) The ratio of cell delamination (from 20 to 30 h APF; control: four nota, versus *Catalase*: three nota under the control of *Pnr-Gal4*). The p value was calculated by an unpaired two-tailed Student's t test. n.s., not significant and **, p < 0.01. Error bars indicate standard error of the mean.

(C) Diagram of CaspaseTRACKER.

(D and F) Snapshots from the movie, z-projections and y-projections of confocal stacks in the pupal notum of a live fly expressing and *Ecad::GFP* with *CasT* at 25 (D) and 31 h APF (F). Arrowheads and arrows indicate delaminating cells and cell fragmentation in delamination, respectively (F).

(E) Distribution of CasT$^+$ cells that delaminated in the hours from 25 to 31 h APF (three nota, 71 cells). Error bars indicate standard error of the mean.

(G and H) The ratio of CasT$^+$ cell delamination (G) and fragmentation in delamination (H) for 6 h (control: three nota, versus *Catalase* or *p35*: three nota under the control of *Pnr-Gal4*). The p value was calculated by one-way analysis of variance (ANOVA) with Dunnett's test. n.s., not significant, *, p < 0.05, **, p < 0.01, and ***, p < 0.005. Error bars indicate standard error of the mean.

(I) A snapshot from the movie, z-projections of confocal stacks in the pupal notum of a live fly expressing *Ecad::GFP* after the injection of a mixture of propidium iodide (PI) and Hoechst 33342. A magnified image of delaminating cells stained (I') or unstained (I'') with PI as shown in coronal and sagittal sections.

(J) The ratio of PI$^+$ cells to delaminating cells (from 18 ± 2 to 40 ± 2 h APF; three nota, 230 cells). Error bar indicates standard error of the mean.

The boundaries between the midline (M) and outside the midline (OM) regions are outlined with dotted white lines. The anterior-to-posterior axes of all pupae are oriented toward the left. Scale bars: 10 μm.

See also Figures S4–S6 and Video S2 and Video S3.

## H$_2$O$_2$ Prevents Delaminating Cells from Apoptotic Nuclear Fragmentation

Next, we found that less than 10% of the delaminating CasT$^+$ cells showed nuclear fragmentation, a feature of typical apoptosis (Figures 6F and 6H, Video S2). In addition, the injection of a marker of late apoptosis, namely, propidium iodide (PI), into the pupa revealed that only 4.3% of the delaminating cells turned PI-positive (Figures 6I and 6J, Video S3). These results suggest that, although caspase-3 is activated in delaminating cells, this activation could be insufficient for executing apoptotic cell death. When *Catalase* was expressed in CasT$^+$ cells, nuclear fragmentation was increased (Figures 6F and 6H), supporting the idea that H$_2$O$_2$ inhibits events occurring after initial caspase-3 activation (such as nuclear fragmentation). Therefore, cells undergo delamination without apparent apoptotic features. Taking this into consideration, the presence of both O$^-_2$ and intracellular H$_2$O$_2$ before and after caspase-3 activation leads to live cell delamination (Figure 7).

DISCUSSION

Caspase-activated cells have been identified in several tissue fusions (Ray and Niswander, 2012). However, the regulatory mechanisms and functions of caspases are poorly understood. After thorax fusion in *Drosophila*, epithelial crowding induces cell delamination. Here, we showed the regulation of NADPH oxidases for caspase-3 activation and delamination and suggested contrasting controls for caspase-dependent cell delamination via two types of ROS (O$^-_2$ and H$_2$O$_2$). Nox is localized on intracellular membranes (ER or redoxosome) as well as plasma membrane in mammalian cells (Bedard and Krause, 2007; Spencer and Engelhardt, 2014). Distribution of Nox neighboring proteins labeled by Nox::V5::TurboID suggests Nox localization not only on plasma membrane but also on intracellular membranes in M region (Figure S2C'). Thus, the suppressive effect of *Sod1* and *Sod3* on cell delamination indicates the involvement of intracellular and extracellular O$^-_2$ produced by Nox (Figure 7). Duox localizes on plasma membrane and produces O$^-_2$ in the extracellular space. The inhibitory effect of *Duox-RNAi* on cell delamination supports the idea that extracellular O$^-_2$ also promotes cell delamination. However, we could not deny the possibility that extracellular ROS promote cell delamination in a non-cell autonomous fashion.

H$_2$O$_2$ is known to be an activator of redox signaling and is involved in protective cellular functions. This includes an anti-apoptotic role in NF-κB activation (Sies, 2017). Given that the expression of the H$_2$O$_2$ scavenger *Catalase* significantly increased delamination and nuclear fragmentation (Figures 6F–6H), H$_2$O$_2$ likely blocks the events that occur after initial caspase-3 activation. Caspases cleave inhibitor of caspase-activated DNase (ICAD), and activated CAD promotes DNA fragmentation (Enari et al., 1998; Vaux and Korsmeyer, 1999). H$_2$O$_2$-driven oxidation of targets other than caspases, such as DNases like CAD, may affect nuclear fragmentation during delamination. In *Caenorhabditis elegans*, high oxidative stress delayed the appearance of apoptotic corpses (Lin et al., 2016). H$_2$O$_2$ prevents dimer formation of the Endonuclease G (EndoG) homolog CPS-6, which is involved in apoptotic DNA fragmentation, and the oxidized monomeric CPS-6 shows reduced nuclease activity (Lin et al., 2016). Notably, proline (P207) oxidation of EndoG/CPS-6 is suggested to be critical for the dissociation of the dimer into a monomeric form. This residue is conserved in *Drosophila* and humans.
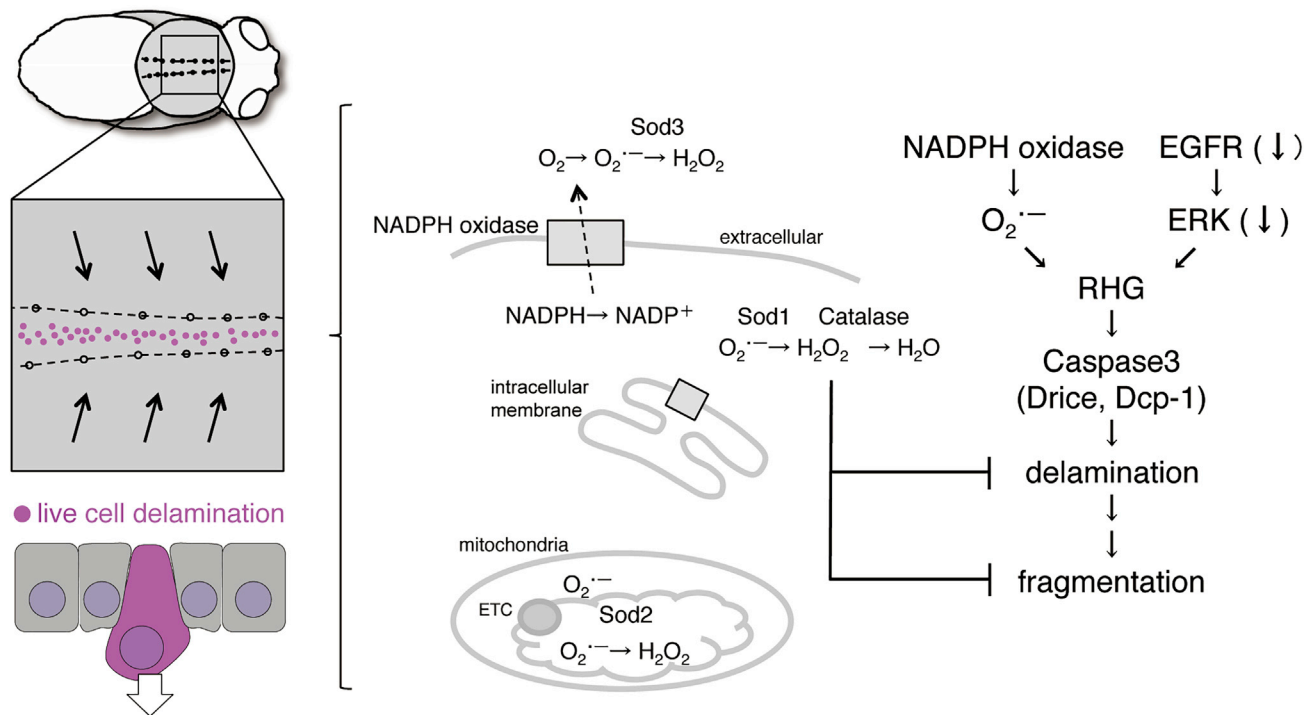
Figure 7. A Model of the Mechanisms of Cell Delamination

Our summarized model for cell delamination in the midline region of *Drosophila* pupal notum. NADPH oxidase is shown as gray square. ETC, electron transfer chain; RHG, Reaper, Hid, and Grim.

MDCK cell extrusion initiated by apoptotic stimulation (caspase-8 activation or UV irradiation) is suppressed by inhibiting the calcium wave (Takeuchi et al., 2020) or via loss of desmosomal junctions (Thomas et al., 2020). Given that these extruding cells do not show apoptotic bodies, a common preventive mechanism could underlie cell fragmentation during M region cell delamination in the *Drosophila* pupal notum. Interestingly, two ROS may regulate distinct extrusion processes, with $O^{\cdot-}_2$ regulating calcium wave or desmosomal reorganization and H_2O_2 preserving the extruding cell shape.

Although most delamination is reported to be independent of caspase activation (Marinari et al., 2012), more detailed observations and genetic manipulations have revealed that apoptotic signaling is required for delamination (Levayer et al., 2016). These discrepant results are likely attributable to Gal4 drivers, specifically *Pnr-Gal4* and the stronger driver *Act-Gal4*, and/or the UAS lines used for caspase inhibition. In the present study, although caspase dependency was confirmed, we still sought to determine whether caspase-dependent delamination is accompanied by apoptosis. Considering the CasT and PI experiments, the integrities of the nuclear and plasma membranes appeared to be intact during delamination (Figures 6D–6J).

In this study, we utilized several live imaging reporters for visualizing *in vivo* signaling events during cell delamination. We briefly summarized how respective reporters can be used for predicting cell delamination in Figure S6F. CasT can preferentially detect transient or weak caspase activation in cells (Figure 6C) but cannot detect apoptotic cells if CasT-cleaved cells are rapidly extruded and/or removed via engulfment before CasT-driven expression of reporter proteins. Although its sensitivity for detecting caspase activation appears to be lower than CasT, we used another indicator for caspase-3 activation (Schott et al., 2017). VC3Ai enables single cell visualization of caspase-3 activation to monitor real-time caspase activation and cell morphological dynamics during delamination (Figure S6A). Live imaging of delamination showed that caspase-3 is indeed activated during delamination (Figures S6B and S6C). Although the real-time reporter VC3Ai appears to be less sensitive to caspase-3 activation than CasT, it can detect the caspase-3 activity required to execute apoptosis (Zhang et al., 2013). Observations with this reporter determined that most VC3Ai^{+} cells in the M region were not fragmented, whereas those in the OM region showed typical apoptotic cell fragmentation (Figures S6D and S6E). The latter cells could be dead before or

immediately after delamination, further highlighting the unique characteristics of caspase-3 activated cells in the M region. These findings also support the fact that the majority of delamination in the M region is live cell extrusion, despite caspase-3 activation (Figure 7).

Moreno et al. revealed that ERK downregulation in the pupal notum does not depend on the Spitz/EGF sequestration factor Argos (Moreno et al., 2019). This suggests that mechanical cues, but not diffusible factors, are involved in cell delamination. Here, we monitored Nox upregulation in delaminating cells. It has been reported that mechanical strain to embryoid bodies from embryonic stem cells induces expression of the NADPH oxidases Nox-1 and Nox-4, along with ROS generation. This leads to ERK1, ERK2, and JNK activation to promote cardiovascular differentiation (Schmelter et al., 2006). Although the involvement of mechanical stress in the EGFR/ERK and Nox pathways is largely unknown, such pathways activating cell survival and/or apoptotic signaling may be broadly used in multicellular organisms. The molecular mechanisms identified here in *Drosophila* may be evolutionarily conserved and may therefore be beneficial for understanding how cell extrusion functions in epithelial tissue development and homeostasis.

Limitation of the Study

We conducted genetic manipulation for ROS generating and scavenging genes to test the involvement of ROS for cell delamination along the midline in the notum. Although our genetic analysis clearly showed the requirement of $O_2^{\cdot-}$-generating enzyme Nox and Duox for delamination, we have not detected the changes in the levels of $O_2^{\cdot-}$ during delamination. Given that $O_2^{\cdot-}$ has short lifetime, the detection of $O_2^{\cdot-}$ at the single cell level was technically very difficult. Thus, we cannot deny the possibility that Nox and/or Duox regulates delamination independent of $O_2^{\cdot-}$ generation. H_2O_2 is relatively stable, and the *GstD-GFP* reporter can be used for detection of accumulation of H_2O_2. Again, however, we could not exactly reveal the dynamics of H_2O_2 at the single cell level over time. Therefore, it is necessary to develop the monitoring technique for the dynamics of ROS with high spatiotemporal resolution to prove the differential associations of $O_2^{\cdot-}$ and H_2O_2 with cell delamination *in vivo*.

Resource Availability

Lead Contact

Further information and requests for resources and reagents should be directed to and will be fulfilled by the Lead Contact, Masayuki Miura (miura@mol.f.u-tokyo.ac.jp).

Materials Availability

Materials and protocols used in this study are available from the authors upon request.

METHODS

All methods can be found in the accompanying Transparent Methods supplemental file.

SUPPLEMENTAL INFORMATION

Supplemental Information can be found online at https://doi.org/10.1016/j.isci.2020.101413.

ACKNOWLEDGMENTS

AUTHOR CONTRIBUTIONS

Y.F. and M.M. conceived this study. Y.F. and M.M. designed the experiments. Y.F. and N.S. performed the experiments and analyzed the data. M.M. and T.C. supervised the study. Y.F., N.S., T.C., and M.M. wrote the manuscript. All authors have edited and approved the final manuscript.

DECLARATIONS OF INTERESTS

The authors declare no competing or financial interests.

REFERENCES

Bedard, K., and Krause, K.H. (2007). The NOX family of ROS-generating NADPH oxidases: physiology and pathophysiology. Physiol. Rev. *87*, 245–313.

Branon, T.C., Bosch, J.A., Sanchez, A.D., Udeshi, N.D., Svinkina, T., Carr, S.A., Feldman, J.L., Perrimon, N., and Ting, A.Y. (2018). Efficient proximity labeling in living cells and organisms with TurboID. Nat. Biotechnol. *36*, 880–887.

Cuervo, R., and Covarrubias, L. (2004). Death is the major fate of medial edge epithelial cells and the cause of basal lamina degradation during palatogenesis. Development *131*, 15–24.

Cuervo, R., Valencia, C., Chandraratna, R.A.S., and Covarrubias, L. (2002). Programmed cell death is required for palate shelf fusion and is regulated by retinoic acid. Dev. Biol. *245*, 145–156.

Ding, A.X., Sun, G., Argaw, Y.G., Wong, J.O., Easwaran, S., and Montell, D.J. (2016). CasExpress reveals widespread and diverse patterns of cell survival of caspase-3 activation during development in vivo. Elife *5*, e10936.

Eisenhoffer, G.T., Loftus, P.D., Yoshigi, M., Otsuna, H., Chien, C.B., Morcos, P.A., and Rosenblatt, J. (2012). Crowding induces live cell extrusion to maintain homeostatic cell numbers in epithelia. Nature *484*, 546–549.

Enari, M., Sakahira, H., Yokoyama, H., Okawa, K., Iwamatsu, A., and Nagata, S. (1998). A caspase-activated DNase that degrades DNA during apoptosis, and its inhibitor ICAD. Nature *391*, 43–50.

Evans, C.J., Olson, J.M., Ngo, K.T., Kim, E., Lee, N.E., Kuoy, E., Patananan, A.N., Sitz, D., Tran, P., Do, M.T., et al. (2009). G-TRACE: rapid Gal4-based cell lineage analysis in Drosophila. Nat. Methods *6*, 603–605.

Farbman, A.I. (1968). Electron microscope study of palate fusion in mouse embryos. Dev. Biol. *18*, 93–116.

Fujisawa, Y., Kosakamoto, H., Chihara, T., and Miura, M. (2019). Non-apoptotic function of *Drosophila* caspase activation in epithelial thorax closure and wound healing. Development *146*, dev160937.

Hinrichsen, K. (1985). The early development of morphology and patterns of the face in the human-embryo. Adv. Anat. Embryol. Cell *98*, 1–76.

Kansanen, E., Kuosmanen, S.M., Leinonen, H., and Levonen, A.L. (2013). The Keap1-Nrf2 pathway: mechanisms of activation and dysregulation in cancer. Redox Biol. *1*, 45–49.

Koto, A., Kuranaga, E., and Miura, M. (2011). Apoptosis ensures spacing pattern formation of *Drosophila* sensory organs. Curr. Biol. *21*, 278–287.

Lee, P.T., Zirin, J., Kanca, O., Lin, W.W., Schulze, K.L., Li-Kroeger, D., Tao, R., Devereaux, C., Hu, Y.H., Chung, V., et al. (2018). A gene-specific T2A-GAL4 library for *Drosophila*. Elife *7*, e35574.

Levayer, R., Dupont, C., and Moreno, E. (2016). Tissue crowding induces caspase-dependent competition for space. Curr. Biol. *26*, 670–677.

Li, W., Young, J.F., and Sun, J.J. (2018). NADPH oxidase-generated reactive oxygen species in mature follicles are essential for *Drosophila* ovulation. Proc. Natl. Acad. Sci. U S A *115*, 7765–7770.

Lin, J.L.J., Nakagawa, A., Skeen-Gaar, R., Yang, W.Z., Zhao, P., Zhang, Z., Ge, X., Mitani, S., Xue, D., and Yuan, H.S. (2016). Oxidative stress impairs cell death by repressing the nuclease activity of mitochondrial endonuclease G. Cell Rep. *16*, 279–287.

Marinari, E., Mehonic, A., Curran, S., Gale, J., Duke, T., and Baum, B. (2012). Live-cell delamination counterbalances epithelial growth to limit tissue overcrowding. Nature *484*, 542–545.

Martin-Blanco, E., and Knust, E. (2001). Epithelial morphogenesis: filopodia at work. Curr. Biol. *11*, R28–R31.

Martin-Blanco, E., Pastor-Pareja, J.C., and Garcia-Bellido, A. (2000). JNK and decapentaplegic signaling control adhesiveness and cytoskeleton dynamics during thorax closure in *Drosophila*. Proc. Natl. Acad. Sci. U S A *97*, 7888–7893.

Martinez-Alvarez, C., Tudela, C., Perez-Miguelsanz, J., O'Kane, S., Puerta, J., and Ferguson, M.W.J. (2000). Medial edge epithelial cell fate during palatal fusion. Dev. Biol. *220*, 343–357.

Moreno, E., Valon, L., Levillayer, F., and Levayer, R. (2019). Competition for space induces cell elimination through compaction-driven ERK downregulation. Curr. Biol. *29*, 23–34 e8.

Mori, C., Nakamura, N., Okamoto, Y., Osawa, M., and Shiota, K. (1994). Cytochemical identification of programmed cell-death in the fusing fetal mouse palate by specific labeling of DNA fragmentation. Anat. Embryol. *190*, 21–28.

Ray, H.J., and Niswander, L. (2012). Mechanisms of tissue fusion during development. Development *139*, 1701–1711.

Redza-Dutordoir, M., and Averill-Bates, D.A. (2016). Activation of apoptosis signalling pathways by reactive oxygen species. Biochim. Biophys. Acta *1863*, 2977–2992.

Schmelter, M., Ateghang, B., Helmig, S., Wartenberg, M., and Sauer, H. (2006). Embryonic stem cells utilize reactive oxygen species as transducers of mechanical strain-induced cardiovascular differentiation. Faseb J. *20*, 1182.

Schott, S., Ambrosini, A., Barbaste, A., Benassayag, C., Gracia, M., Proag, A., Rayer, M., Monier, B., and Suzanne, M. (2017). A fluorescent toolkit for spatiotemporal tracking of apoptotic cells in living *Drosophila* tissues. Development *144*, 3840–3846.

Sies, H. (2017). Hydrogen peroxide as a central redox signaling molecule in physiological oxidative stress: oxidative eustress. Redox Biol. *11*, 613–619.

Spencer, N.Y., and Engelhardt, J.F. (2014). The basic biology of redoxosomes in cytokine-mediated signal transduction and implications for disease-specific therapies. Biochemistry *53*, 1551–1564.

Suzuki, T., Muramatsu, A., Saito, R., Iso, T., Shibata, T., Kuwata, K., Kawaguchi, S.I., Iwawaki, T., Adachi, S., Suda, H., et al. (2019). Molecular mechanism of cellular oxidative stress sensing by Keap1. Cell Rep. *28*, 746–758 e744.

Sykiotis, G.P., and Bohmann, D. (2008). Keap1/Nrf2 signaling regulates oxidative stress tolerance and lifespan in *Drosophila*. Dev. Cell *14*, 76–85.

Takemoto, K., Nagai, T., Miyawaki, A., and Miura, M. (2003). Spatio-temporal activation of caspase revealed by indicator that is insensitive to environmental effects. J. Cell Biol. *160*, 235–243.

Takeuchi, Y., Narumi, R., Akiyama, R., Vitiello, E., Shirai, T., Tanimura, N., Kuromiya, K., Ishikawa, S., Kajita, M., Tada, M., et al. (2020). Calcium wave promotes cell extrusion. Curr. Biol. *30*, 670–681.e6.

Tang, H.L., Tang, H.M., Fung, M.C., and Hardwick, J.M. (2015). In vivo CaspaseTracker biosensor system for detecting anastasis and non-apoptotic caspase activity. Sci. Rep. *5*, 9015.

Thomas, M., Ladoux, B., and Toyama, Y. (2020). Desmosomal junctions govern tissue integrity and actomyosin contractility in apoptotic cell extrusion. Curr. Biol. *30*, 682–690.e5.

Vaux, D.L., and Korsmeyer, S.J. (1999). Cell death in development. Cell *96*, 245–254.

Wang, Y., Branicky, R., Noe, A., and Hekimi, S. (2018). Superoxide dismutases: dual roles in controlling ROS damage and regulating ROS signaling. J. Cell Biol. *217*, 1915–1928.

Xie, H.T., Wan, Z.Y., Li, S., and Zhang, Y. (2014). Spatiotemporal production of reactive oxygen species by NADPH Oxidase is critical for tapetal programmed cell death and pollen development in Arabidopsis. Plant Cell *26*, 2007–2023.

Yamaguchi, Y., Shinotsuka, N., Nonomura, K., Takemoto, K., Kuida, K., Yosida, H., and Miura, M. (2011). Live imaging of apoptosis in a novel transgenic mouse highlights its role in neural tube closure. J. Cell Biol. *195*, 1047–1060.

Zhang, J., Wang, X., Cui, W., Wang, W., Zhang, H., Liu, L., Zhang, Z., Li, Z., Ying, G., Zhang, N., et al. (2013). Visualization of caspase-3-like activity in cells using a genetically encoded fluorescent biosensor activated by protein cleavage. Nat. Commun. *4*, 2157.

Supplemental Information

ROS Regulate Caspase-Dependent Cell Delamination

without Apoptosis in the *Drosophila* Pupal Notum

Yuya Fujisawa, Natsuki Shinoda, Takahiro Chihara, and Masayuki Miura

SUPPLEMENTAL FIGURES

A

control for CD	UAS-X	Fly stock	1st	2nd
1	Bsk-RNAi	V34138	CD	
2	Pvr-DN	B58430	CD	
3	Dad	Tsuneizumi et al.	CD	
cell death				
4	RHG-RNAi	Siegrist et al.	Br	O
5	Hid-RNAi	V8269, V30033	Br	O
6	Rpr-RNAi	V12045, V101234	Br	-
7	Grim-RNAi	V21830, V22597	NBr	
8	Bruce-RNAi	V48309, V107620	NBr	
9	Diap1	Hay et al.	Br	O
10	Dark-RNAi	Obata et al.	Br	O
11	Dronc-RNAi	Obata et al.	Br	(O)
12	Dronc-DN	Quinn et al.	Br	-
13	p35	D108019	Br	O
mechano-sensing				
14	Piezo-RNAi	V2796	NBr	
15	Ppk-RNAi	V108683	NBr	
16	Iav-RNAi	V7126, V7128, V100701	NBr	
17	Nan-RNAi	V5261, V100090	NBr	
18	Nompc-RNAi	V105579	NBr	
19	Painless-RNAi	V39477, V39478	NBr	
20	Pkd2-RNAi	V6940, V6941	NBr	
21	Pyx-RNAi	V110130, V35165	NBr	
22	Trp-RNAi	V1365, V1366	NBr	
23	TrpA1-RNAi	V37249	NBr	
24	Trpy-RNAi	V9337, V9338, V105280	NBr	
25	Trpl-RNAi	V104450	NBr	
26	Trpm-RNAi	V33670, V10753	NBr	
27	Trpml-RNAi	V108088	NBr	
28	Wtrw-RNAi	V42617, V42620, V107423	NBr	
29	Rhea-RNAi	V40399	NBr	
30	αcatenin-RNAi	V19182, V20123, V104566	NBr	
31	p130cas-RNAi	V41479	NBr	

cytoskeleton	UAS-X	Fly stock	1st	2nd
32	Merlin-RNAi	V7161, V39177	Br	×
33	Arm-RNAi	V107344	CD	
34	Echinoid-RNAi	V938	NBr	
35	Kibra-RNAi	V106507	NBr	
36	Cherrio-RNAi	V107451	NBr	
37	Vinculin-RNAi	V34585	NBr	
38	p120-RNAi	V103063	NBr	
39	Pak1-RNAi	V12553	NBr	
40	Shg	D107873	NBr	
41	Plexa-RNAi	V4740	NBr	
42	Rock-RNAi	V3793	CD	
ROS				
43	Sod1	B24750, B24754	Br	(O)
44	Sod1-RNAi	V31551, V108307	NBr	
45	Sod2	B24494	Br	(O)
46	Sod2-RNAi	V42162, V110547	NBr	
47	Catalase	B24621	Br	×
48	Catalase-RNAi	V6283, V103591	NBr	
49	Keap1	B15427	Br	×
50	Keap1-RNAi	V107052	NBr	
51	Cnc-RNAi	V108127	NBr	
52	Hayan-RNAi	V28410	Br	×
53	MitoPLD-RNAi	V38626, V106137	NBr	
54	Drp1-RNAi	V44155	NBr	
55	Nox-RNAi	B32902, V4913	Br	O
56	Duox-RNAi	B32903, V2593,	Br	O
other genes				
57	EGFR-CA	Dominguez et al.	CD	
58	Grnd-RNAi	V43454, V104538	NBr	
59	Ptp10d-RNAi	V1101, V1102, V8010	Br	-
60	Sas-RNAi	V100901	NBr	
61	EcR-RNAi	B9327	NBr	
62	Foxo-RNAi	B32427	Br	O
63	Atf3	Sekyrova et al	Br	(O)

B

Pnr> +   *Pnr> Dark-RNAi* ('Br')   *Pnr> Dad* ('CD')
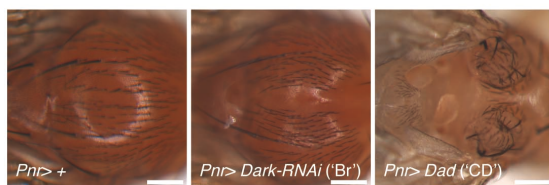
C

NADPH oxidases	UAS-X	Fly stock	1st	2nd
56	Nox-RNAi	B32433	Br	O
		B32902	Br	(O)
		B38906	NBr	
		B38921	Br	(O)
		B50581	NBr	
		V4913	NBr	
		V4914	NBr	
		V100753	NBr	
		V102559	Br	(O)
57	Duox-RNAi	B32903	Br	O
		B38907	Br	O
		B38916	Br	O
		V2593	NBr	

Fig. S1. Related to Fig. 1. Genetic screen for cell delamination

(A) A list of the screening results for genes that were overexpressed or inhibited with UAS lines under the control of *Pnr-Gal4*. Abbreviations of B, V, and D in fly stock were used for the Bloomington *Drosophila* Stock Center (BDSC), the Vienna *Drosophila* Resource Center (VDRC), and the *Drosophila* Genetic Resource Center (DGRC) Kyoto, respectively. Abbreviations for phenotypes in the midline (M) region of adult nota were used in the first screening; CD: closure defected, Br: broaden, and NBr: not-broaden, respectively. Symbols for quantitative results were used in the second screening; ○: cell delamination was > 50% suppressed, (○): cell delamination was significantly suppressed but < 50%, and ×: cell delamination was not suppressed compared to the control. The dash (-) indicates candidates not tested in the second screening. The UAS lines with which each phenotype was induced are underlined in the list. Gene manipulations were categorized into six groups, including control for CD, cell death, mechano-sensing, cytoskeleton, ROS, and other genes. Hit candidates are marked by green. (B) Representative images of the adult notum phenotypes. Compared to the control, *Dark-RNAi* and *Dad* induced Br and CD phenotypes of the M region, respectively. (C) A list of the results especially for *Nox-RNAi* and *Duox-RNAi*. The anterior-to-posterior axes of all adults are oriented toward the left. Scale bars: 100 μm.
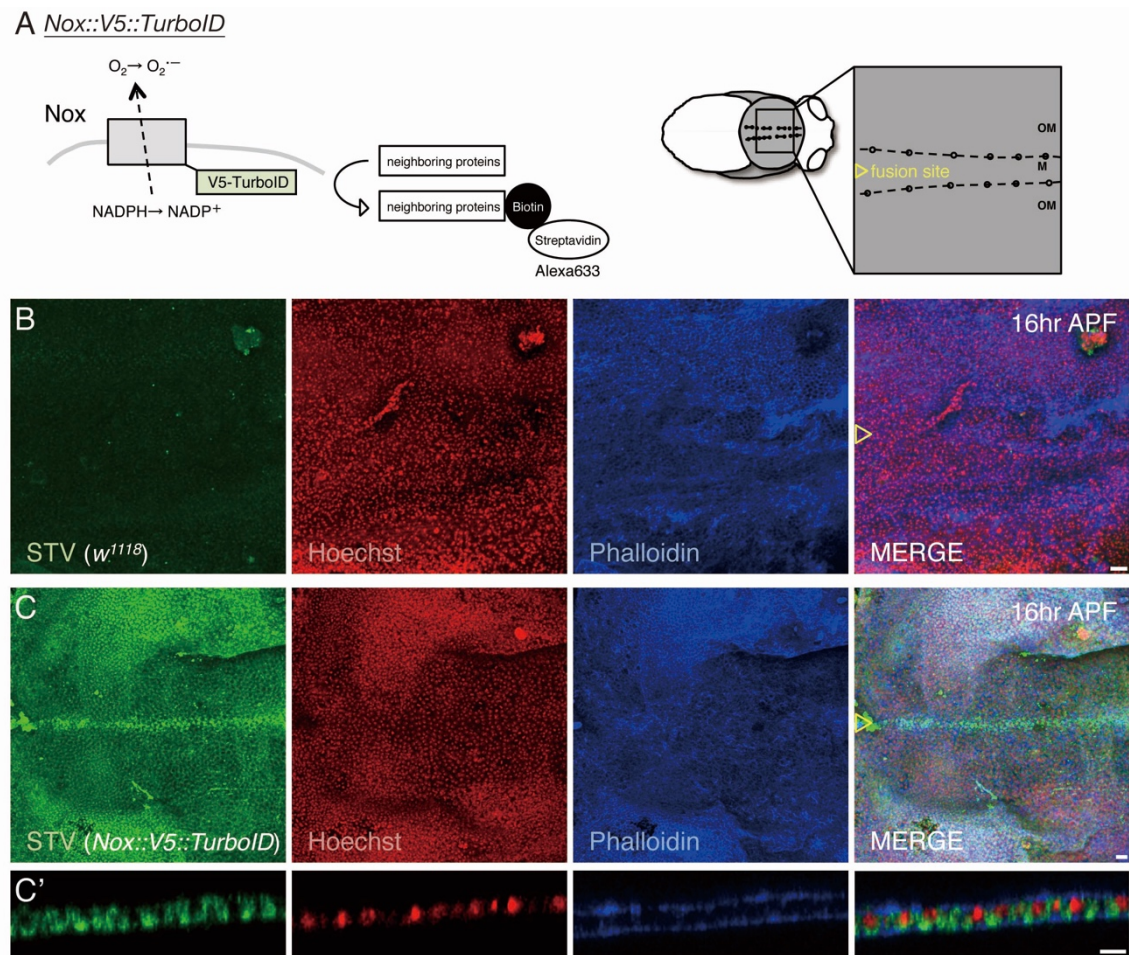
Fig. S2. Related to Fig. 2. TurboID-mediated labeling of neighboring proteins of Nox
(A) A diagram representing Nox::V5::TurboID construction and the system of TurboID. Proteins neighboring Nox are labeled by biotinylation. (B–C) Images of the z-projections of confocal stacks in the pupal notum of a dissected w^{1118} or *Nox::V5::TurboID* fly (16 h after puparium formation; APF). A green image shows biotinylated proteins that were detected by streptavidin (STV)-Alexa 633. The nucleus and F-actin were co-stained with Hoechst33342 (red) and Phalloidin (blue), respectively. (C') A magnified image of the z-section along midline of (C). Yellow arrowhead indicates the fusion site of the thorax closure. The anterior-to-posterior axes of all pupae are oriented toward the left. Scale bars: 10 μm.
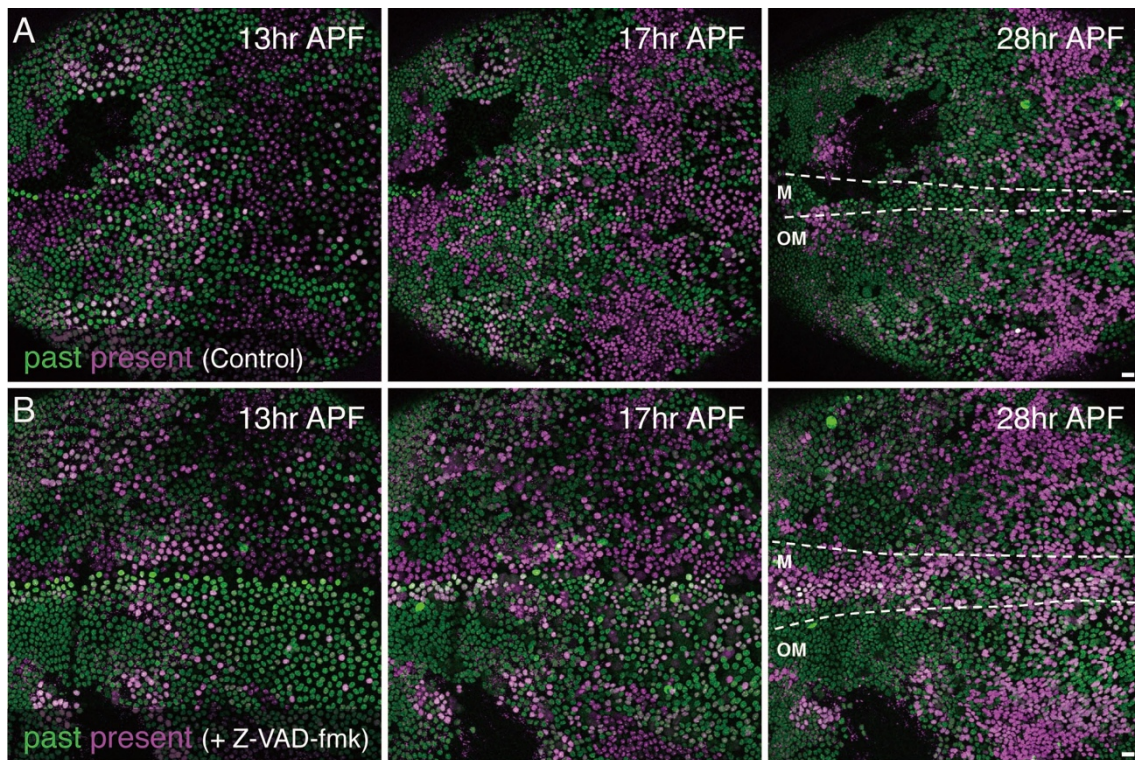
Fig. S3. Related to Fig. 3. Nox functions upstream of caspase-3 activation

(A–B) Snapshots from the movie, z-projections of confocal stacks in the pupal notum of a live fly expressing *Nox-Gal4* and *G-TRACE* (13, 17, and 28 h after puparium formation; APF). Compared to the control, tissues with injected Z-VAD-fmk still showed "present" expression of Nox and a broaden (Br) phenotype of the midline (M) region at 28 h APF due to the absence of cell delamination with "present" Nox expression. The boundaries between the M and outside the midline (OM) regions are outlined with dotted white lines. The anterior-to-posterior axes of all pupae are oriented toward the left. Scale bars: 10 μm.
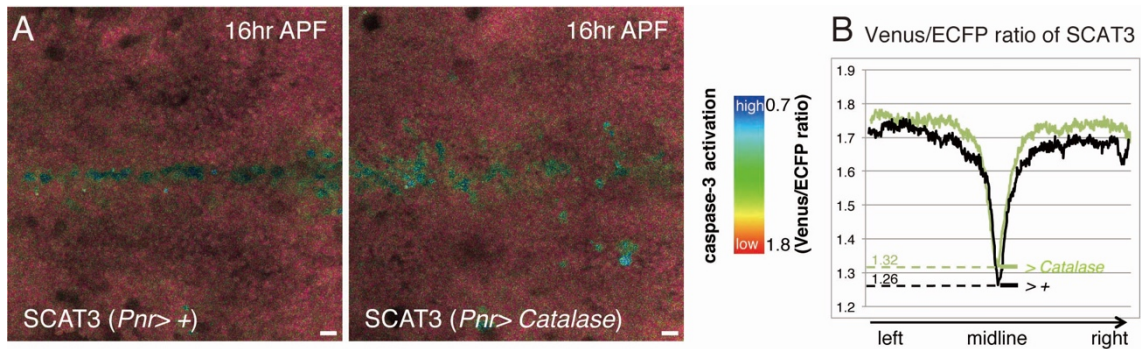
Fig. S4. Related to Fig. 5 and 6. Catalase overexpression does not inhibit caspase-3 activation

(A) Snapshots from the movie, z-projections of confocal stacks in the pupal notum of a live fly expressing SCAT3 under the control of *Pnr-Gal4* (16 h after puparium formation; APF). (B) Averaged changes in the FRET ratio (the Venus signal to the ECFP signal) of SCAT3 (16 h APF; control: four nota, versus *Catalase*: six nota). The anterior-to-posterior axes of all pupae are oriented toward the left. Scale bars: 10 μm.
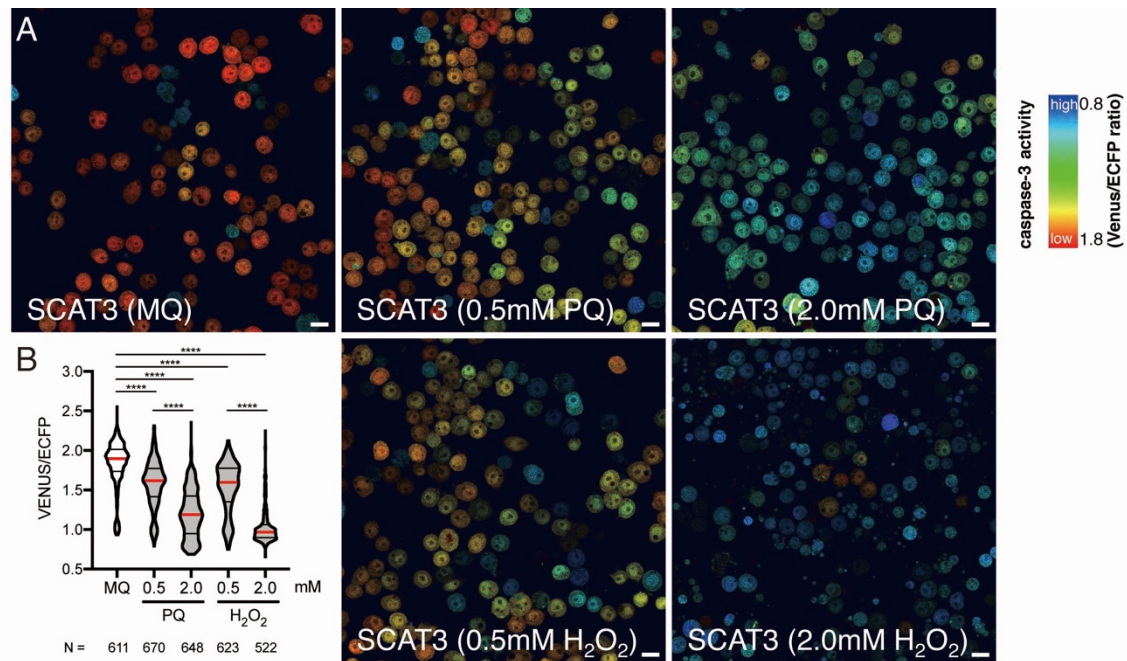
Fig. S5. Related to Fig. 5 and 6. Paraquat (PQ) and H₂O₂ treatment-induced caspase-3 activation

(A) Images of *Drosophila* cultured S2 cells stably expressing SCAT3 16 h after treatment with MilliQ (MQ), 0.5, 2.0 mM PQ, 0.5, 2.0 mM H₂O₂. (B) Changes in the FRET ratio (the Venus signal to the ECFP signal) of SCAT3 (MQ: 611 cells, versus cells treated with reactive oxygen species (ROS), 0.5 mM PQ: 670 cells, 2.0 mM PQ: 648 cells, 0.5 mM H₂O₂: 623 cells, or 2.0 mM H₂O₂: 522 cells). The P value was calculated by Sidak's multiple comparison test. ****$P < 0.0001$. Scale bars: 10 µm.
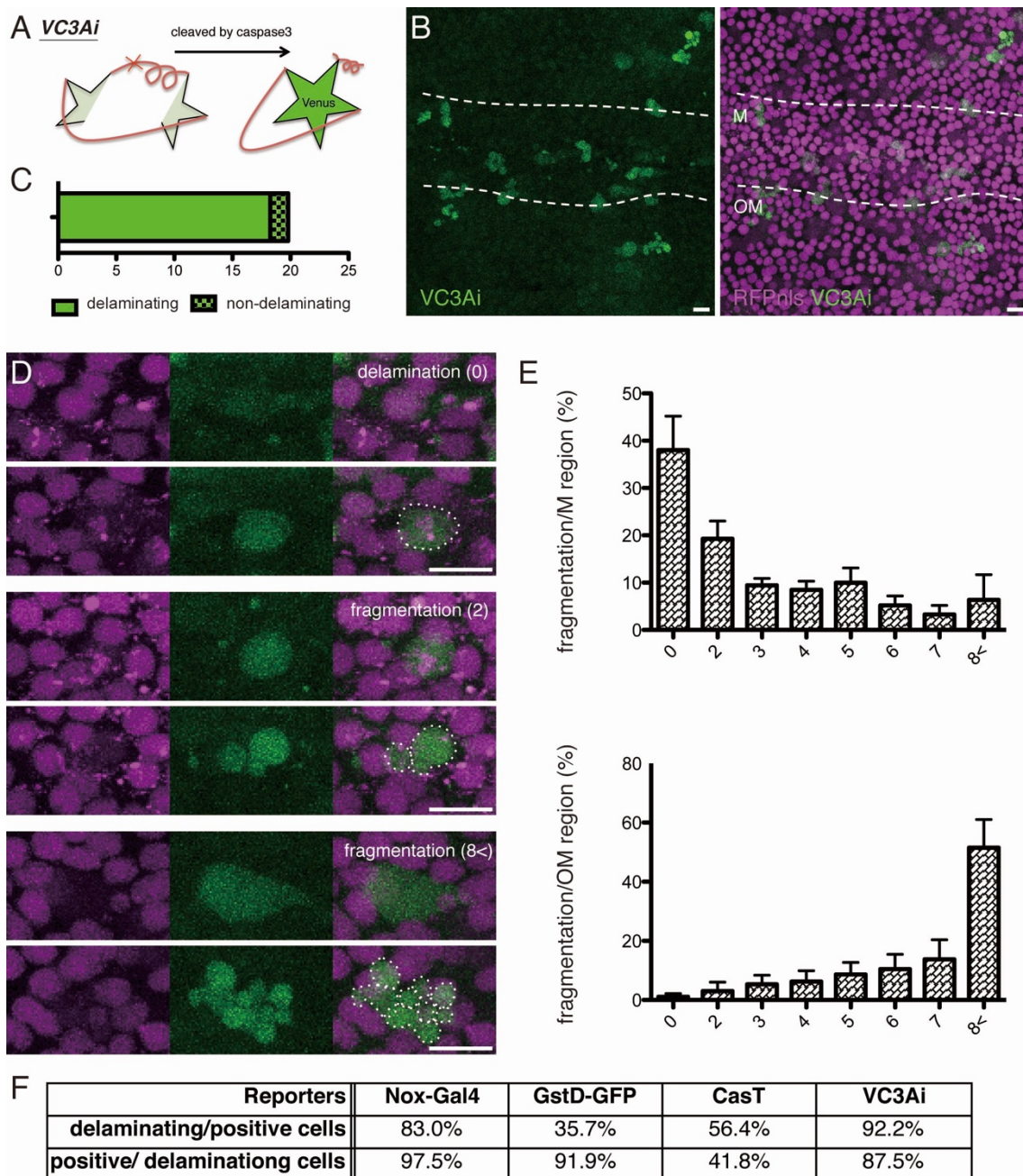
Fig. S6. Related to Fig. 6. Less cell fragmentation in caspase-3 activated cells of the midline (M) region

(A) VC3Ai construction. (B,D) Snapshots from the movie, z-projections of confocal stacks in the pupal notum of a fly expressing VC3Ai under the control of *Ap-Gal4* and RFP::nls ubiquitously. (C) The ratio of the number of VC3Ai^{+} cells that delaminated in

the M region for 10 hours (from 15.5 ± 2-26 ± 1 h after puparium formation; APF; three nota, 389 cells). (E) The ratio of the number of cell fragments in VC3Ai$^+$ cells that delaminated for 8 hours (from 17-25 h APF; four nota: M = 111 cells, versus outside the midline (OM) = 62 cells). The boundary between the M and OM regions is outlined with dotted white lines. The anterior-to-posterior axis of the pupa is oriented toward the left. Scale bars: 10 µm. (F) The prevalence of each indicator during cell delamination event.

TRANSPARENT METHODS

KEY RESOURCES TABLE

LEAD CONTACT AND MATERIALS AVAILABILITY

EXPERIMENTAL MODEL AND SUBJECT DETAIL

- Fly Stocks and Cultivation

- Genotype Details

METHOD DETAILS

- Time-lapse Record

- Delamination Rate

- FRET Image

- Intensity Profile

- Mosaic Analysis

- Subcellular Distribution

- Drug Injection

- Phenotype Screen

- DNA Construction

- Biotinylation Method

- Histological Analysis

- Cell Culture Assays

- Cell Fragmentation

QUANTIFICATION AND STATISTICAL ANALYSIS

SUPPLEMENTAL REFERENCES

KEY RESOURCES TABLE

REAGENT or RESOURCE	SOURCE	IDENTIFIER
Chemicals, Peptides, and Recombinant Proteins		
DHE	Invitrogen	D11347
propidium iodide (PI)	Sigma	P4170
Streptavidin (STV) Alexa Fluor 633-conjugate	Invitrogen	S21375
Hoechst33342	Invitrogen	H3570
Rhodamine Phalloidin Alexa Fluor 488-conjugate	Invitrogen	A12379
Z-VAD-fmk	Sigma-Aldrich	627610
Schneider's *Drosophila* medium	Gibco	21720-024

fetal bovine serum	Thermo Fisher Scientific	SH30910.03
streptomycin	Wako	168-23191
Effectene Transfection Reagent	QIAGEN	301427
Hygromycin B	Wako	084-07681
Paraquat (PQ)	Sigma-Aldrich	36541
H_2O_2	Wako	081-04215
Experimental Models: Organisms/Strains		
D. melanogaster: Ubi-Ecad::GFP	DGRC	109007
D. melanogaster: Pnr-Gal4	BDRC	3039
D. melanogaster: UAS-Diap1	(Hay et al., 1995)	N/A
D. melanogaster: UAS-RHG-RNAi	(Siegrist et al., 2010)	N/A
D. melanogaster: UAS-Hid-RNAi	VDRC	8269
D. melanogaster: UAS-Dark-RNAi	(Obata et al., 2014)	N/A
D. melanogaster: UAS-Dronc-RNAi	(Obata et al., 2014)	N/A
D. melanogaster: UAS-p35	DGRC	108019
D. melanogaster: UAS-Nox-RNAi	BDRC	32433
D. melanogaster: UAS-Nox-RNAi	BDRC	32902
D. melanogaster: UAS-Nox-RNAi	BDRC	38921
D. melanogaster: UAS-Nox-RNAi	VDRC	102559
D. melanogaster: UAS-Duox-RNAi	BDRC	32903
D. melanogaster: UAS-Duox-RNAi	BDRC	38907
D. melanogaster: UAS-Duox-RNAi	BDRC	38916
D. melanogaster: UAS-SCAT3	(Kanuka et al., 2005)	N/A
D. melanogaster: {CRIMIC}Nox-Gal4	BDRC	78988
D. melanogaster: UAS-DsRed::nls, UAS-Flp, Ubi-FRT-stop-FRT-nuc::EGFP (G-TRACE)	BDRC	28280
D. melanogaster: Hs-flp	BDRC	23649
D. melanogaster: Act-FRT-y+-FRT-Gal4 (Ay-Gal4) UAS-GFP	BDRC	4411
D. melanogaster: Tub-nls::C1C2Cic::mCherry (miniCic)	(Moreno et al., 2019)	N/A
D. melanogaster: GstD-GFP	(Sykiotis and Bohmann, 2008)	N/A
D. melanogaster: Ecad::tdTomato	BDRC	58789
D. melanogaster: UAS-Sod1	BDSC	24754
D. melanogaster: UAS-Sod2	BDRC	24494
D. melanogaster: UAS-Sod3	FlyORF	2420

D. melanogaster: UAS-Catalase	BDRC	24621
D. melanogaster: Caspase-sensitive Gal4 (CaspaseTracker)	(Tang et al., 2015)	N/A
D. melanogaster: UAS-mCherry::nls	BDSC	38424
D. melanogaster: UAS-Dad	(Tsuneizumi et al., 1997)	N/A
D. melanogaster: UAS-Dronc-DN	(Quinn et al., 2000)	N/A
D. melanogaster: UAS-EGFR-CA	(Dominguez et al., 1998)	N/A
D. melanogaster: UAS-Atf3	(Sekyrova et al., 2010)	N/A
D. melanogaster: Nox::V5::TurboID	This paper	N/A
D. melanogaster: Ap-Gal4	BDRC	3041
D. melanogaster: FRT82B Ubi-RFP::nls	BDRC	30555
D. melanogaster: UAS-VC3Ai	(Schott et al., 2017)	N/A
Oligonucleotides		
Primers for plasmid construction, see method details	This paper	Method details
Software and Algorithms		
Leica Application Suite X	Leica Microsystems	N/A
ImageJ	National Institutes of Health	N/A
Metamorph	Molecular Devices	N/A
Prism	Graphpad	N/A

LEAD CONTACT AND MATERIALS AVAILABILITY

Further information and requests for resources and reagents should be directed to and will be fulfilled by the Lead Contact, Masayuki Miura (miura@mol.f.u-tokyo.ac.jp).

EXPERIMENTAL MODEL AND SUBJECT DETAIL
Fly Stocks and Cultivation

All crosses were carried out at 25 °C unless otherwise noted. All strains used in this study were listed in the Key Resources Table.

Genotype Details
Fig. 1C–E
Ubi-Ecad::GFP/+; Pnr-Gal4/+
Ubi-Ecad::GFP/UAS-RHG-RNAi; Pnr-Gal4/+
Ubi-Ecad::GFP/+; Pnr-Gal4/UAS-Hid-RNAi
UAS-Diap1/+; Ubi-Ecad::GFP/+; Pnr-Gal4/+
Ubi-Ecad::GFP/+; Pnr-Gal4/UAS-Dark-RNAi

Ubi-Ecad::GFP/+; Pnr-Gal4/UAS-Dronc-RNAi

Ubi-Ecad::GFP/UAS-p35; Pnr-Gal4/+

Fig. 2A–B

Ubi-Ecad::GFP/+; Pnr-Gal4/+

Ubi-Ecad::GFP/+; Pnr-Gal4/UAS-Nox-RNAi (#B32433)

Ubi-Ecad::GFP/+; Pnr-Gal4/UAS-Duox-RNAi (#B32903)

Fig. 2C-D

UAS-SCAT3/+; Pnr-Gal4/+

UAS-SCAT3/+; Pnr-Gal4/UAS-Nox-RNAi (#B32433)

UAS-SCAT3/+; Pnr-Gal4/UAS-Dark-RNAi

UAS-SCAT3/+; Pnr-Gal4/UAS-Duox-RNAi (#B32903)

Fig. 3B–C

Nox-Ga4/G-TRACE

Fig. 4A–B

Hs-flp/UAS-EGFR-CA; Ay-Gal4 UAS-GFP/miniCic

Hs-flp/+ or Y; Ay-Gal4 UAS-GFP/miniCic; UAS-Nox-RNAi (#B32433) */+*

Hs-flp/+ or Y; Ay-Gal4 UAS-GFP/miniCic

Fig. 4C–D

miniCic/+; Pnr-Gal4/+

miniCic/+; Pnr-Gal4/UAS-Nox-RNAi (#B32433)

Fig. 5A–C

Ecad::tdTomato/GstD-GFP

Fig. 5E–F

Ubi-Ecad::GFP

Fig. 5G–H

Ubi-Ecad::GFP/+; Pnr-Gal4/+

Ubi-Ecad::GFP/UAS-Sod1; Pnr-Gal4/+

Ubi-Ecad::GFP/UAS-Sod2; Pnr-Gal4/+

Ubi-Ecad::GFP/+; Pnr-Gal4/UAS-Sod3

Fig. 5I–J

UAS-SCAT3/+; Pnr-Gal4/+

UAS-SCAT3/UAS-Sod1; Pnr-Gal4/+

UAS-SCAT3/UAS-Sod2; Pnr-Gal4/+

UAS-SCAT3/+; Pnr-Gal4/UAS-Sod3

Fig. 5K

See Fig. 2C–D and Fig. 5I–J.

Fig. 6A–B

Ubi-Ecad::GFP/+; Pnr-Gal4/+

Ubi-Ecad::GFP/+; Pnr-Gal4/UAS-Catalase

Fig. 6D–H

Ubi-Ecad::GFP/CaspaseTracker; UAS-mCherry::nls/+

CaspaseTracker/UAS-Catalase; UAS-mCherry::nls/+

CaspaseTracker/UAS-p35; UAS-mCherry::nls/+

Fig. 6I–J

Ubi-Ecad::GFP

Fig. S1

See Fig. S1.

Fig. S2B

w^{1118}

Fig. S2C–C'

Nox::V5::TurboID/+

Fig. S3A–B

Nox-Ga4/G-TRACE

Fig.S4A–B

UAS-SCAT3/+; Pnr-Gal4/+

UAS-SCAT3/UAS-Catalase; Pnr-Gal4/+

Fig. S6B

Ap-Gal4/+; UAS-VC3Ai/FRT82B Ubi-RFP::nls

Fig. S6C

UAS-VC3Ai/+, Ecad::tdTomato/Pnr-Gal4

Fig. S6D–E

Ap-Gal4/+; UAS-VC3Ai/FRT82B Ubi-RFP::nls

Movie 1

Nox-Ga4/G-TRACE

Movie 2

Ubi-Ecad::GFP/CaspaseTracker; UAS-mCherry::nls/+

Movie 3

Ubi-Ecad::GFP

METHOD DETAILS

Time-lapse Record

Most sampling steps for pupal imaging are described in detail in a previous study (Koto et al., 2009). After staging, live pupae were mounted on glass slides without a part of the pupal case. A drop of water was then applied to fill the space between the pupal thorax and coverslip. Time-lapse images were taken every 5-60 min with a Leica TCS SP5 or SP8 confocal microscope (Leica Microsystems, Wetzlar, Germany) using a 40× (oil) objective at 20 ± 2 °C. In most cases, the pupae developed into adults after imaging. The midline (M) and regions outside the midline (OM) were defined as the region delimited by the two most central lines of bristles, as reported previously (Levayer et al., 2016; Fig. 1A). The center horizontal lines of all images were taken in accordance with the midline of the pupal nota. The same region of each pupal nota was taken along the anterior-posterior axis whenever possible, judging from the position of macrochaete bristles.

Delamination Rate

To quantify the rate of cell delamination, a method used in previous studies was applied (Koto et al., 2011; Levayer et al., 2016; Marinari et al., 2012). The number of delaminating cells was counted and normalized to the initial number of cells in the M region. The delaminating cells were counted by monitoring apical contraction and loss of Ecad::GFP or Ecad::tdTomato (Fig. 1D, 2B, 5B,C,H, and 6B,J), and by estimating the loss of DsRed::nls, nuc::GFP, or mCherry::nls (Fig. 3C, and 6E,G). The experiments depicted in Fig. 1D, 2B, 5H, and 6B were performed almost simultaneously. Therefore, only a single control experiment was used.

FRET Image

Changes in the FRET ratio of SCAT3 were calculated as the ratio of the Venus signal to the ECFP signal (Fig. 2D, 5J,K, and S4B) (Takemoto et al., 2003). Images were analyzed using MetaMorph and ImageJ64. The Venus/ECFP ratio was quantified using Fiji (ImageJ) software (NIH) (Fig. S5B). Images were analyzed automatically using the ImageJ macro. Briefly, the ECFP channel was filtered by the "Gaussian Blur (sigma = 1)", processed with "Auto Threshold ("Triangle" method)", processed with "Watershed", and processed with "Analyze particles (size = 40-200 μm^2, circularity = 0.2-1.0)" to define the region of interest (ROI). Regarding the given ROI, average ECFP and Venus intensities were respectively measured, and the Venus/ECFP ratio was calculated. Statistical analysis was then performed using GraphPad Prism 8. Ratio images were generated using MetaMorph.

Intensity Profile

The "Plot Profile" tool in ImageJ was used to obtain a two-dimensional graph of the pixel intensities along a line within the image (Fig. 2D, 5F,J, and S4B). In each graph, the x-axis and y-axis indicate the distance along the vertical line from the top line of the image (left side of the pupal notum, Fig. 2D) and the average pixel intensity, respectively. Y-axis values show the relative ratio of Venus intensity to the ECFP intensity of SCAT3.

Mosaic Analysis

Hs-flp Ay-Gal4 clones were induced by heat-shock (37 °C) for 10-15 min (Fig. 4A). At 72 h and 24-48 h after heat-shock at the larval stage, images of *Nox-RNAi* and *EGFR-CA* were taken at 16 h APF.

Subcellular Distribution

For Fig. 4A and 4C, the same region was considered along the anterior-posterior axis whenever possible, judging from the positions of macrochaete bristles. To obtain Fig. 4B and 4D, mCherry localization patterns were categorized into three types including cytoplasmic, uniform, and nuclear. Representative images are shown in Fig. 4A.

Drug Injection

Most injection protocols were described in detail in a previous study (Chiba et al., 2019). For Fig. 5E, 6I, and S3B, 0.2-0.5 µL of 1:1 DMSO stock solution with 2.5 mM DHE, 3 mM PI, or 4 mM Z-VAD-fmk and 4 mM Hoechst33342, respectively, was injected into pupae with a glass capillary. At the final phase of live imaging in Fig. 6I, we induced epithelial wounding by laser ablation to confirm the PI circulation. The nuclei of wounded cells immediately turned PI-positive (Movie 3), confirming that the PI was still sufficiently circulating in the tissue.

Phenotype Screen

We first selected the gene manipulations in which adult nota showed a similar phenotype ("Br") to those with inhibited apoptotic signaling (Fig. S1A,C). For all manipulations, > 5 individuals were observed, although no quantification was performed. In the second screening, gene manipulations resulting in defective thorax closure, described as "CD" in Fig. S1A-B, were intentionally removed from the candidates.

DNA Construction

V5::TurboID was inserted at the 3′ end of Nox-coding sequences to generate *Nox::V5::TurboID* knock-in alleles via CRISPR/Cas9-mediated homology-directed repair. Pairs of guide RNAs were identified using the CRISPR Optimal Target Finder tool available on flyCRISPR (http://flycrispr.molbio.wisc.edu/). The DNA fragments for the guide RNAs were subcloned into the *Bbs*I-digested U6b-sgRNA-short vector (a gift from N. Perrimon). The following primers were annealed to generate the DNA fragments for guide RNAs: 5′-TTCGGTACGGATTTGCCTTTCGTA-3′, and 5′-TTCGGTTCTCATTTGCATAAGCAA-3′. To generate the homology-directed repair template, DNA fragments of the 5′ homology arm with V5::TurboID were assembled into the *Bsa*I site, and the DNA fragment of the 3′ homology arm was assembled into the *Sap*I site of pBac[3xP3-DsRed_polyA_Scarless_TK] (Shinoda et al., 2019) using NEBuilder HiFi DNA Assembly (New England Biolabs, Ipswich, MS, USA). The PAM sequences of the gRNA-binding sites in the donor template were mutated to prevent Cas9-directed cleavage following homology-directed repair. The V5::TurboID and DNA fragment were amplified from V5::TurboID-NES_pCDNA3 (#107169, Addgene, Watertown, MS, USA) and the genome DNA of w^{1118} by PCR, using the following primers: (i) forward primer_1, 5′-CGTAAAGAGTGCTTCGGCAAGCCCATCCCCAACCCCC-3′, and reverse primer_1, 5′-GGGCGGAGAAATCAGTCTGCGGTCTGCCGAAAAGCTGCAG-3′, (ii) forward primer_2, 5′-TGAAGGTCTCCTTAATGGATCAACAGGGATCAAAG-3′, and reverse primer_2, 5′-CCAGTACGGATTTGCCTTTCGTAAAGAGTGCTTC-3′, (iii) forward primer_3, 5′-GCCGAAAAGCTGCAGTGATGAACAAGCCGCCACATCCATCGCCCACATCTTC TCGTCCAGTTTCATCTCCACACCACTCGCTCTGTGTCAATCCCCTTC-3′, and reverse primer_3, 5′-GCCGCCACATCCATCGCCCACATCTTCTCGTCCAGTTTCATCTCCACACCACT CGCTCTGTGTCAATCCCCTTCGTTCATCGTTTAACCCTAGAAAGA-3′, and (iv) forward primer_4, 5′-TCTTTCTAGGGTTAAGTTCTCATTTGCATAAGCAACAGGTTTATTTCGGG-3′, and reverse primer_4, 5′-CCTCAATCTGCGTGTGTACCATAATGAAGAGCCGTC-3′. The detailed plasmid DNA sequences are available upon request. The transgenic flies were generated by BestGene Inc. Each DsRed-positive transformant was isogenized and confirmed by genomic PCR.

For pAc5.1-SCAT3 construction, *Bam*HI/*Hin*dIII fragment of pcDNA3-SCAT3 (Takemoto et al., 2003) was blunted and was inserted at the *Eco*RV site of pAc5.1 (gift from Kuranaga E and Nakamura Y).

Biotinylation Method

Larvae were raised in 100 μM biotin containing standard *Drosophila* medium (Fig. S2B–C').

Histological Analysis

For histological analysis (Fig. S2B-C'), pupal nota were dissected and fixed with 4% formaldehyde in phosphate-buffered saline (PBS). Pupal nota were then washed in PBS plus 0.1% Triton X-100 (PBST), followed by incubation for 2 h with streptavidin (STV) Alexa Fluor 633 conjugate (1:200), Hoechst33342 (1:1000), and Rhodamine Phalloidin Alexa Fluor 488 conjugate (1:200).

Cell Culture Assays

For cell culture (Fig. S5A), *Drosophila* S2 cells were grown at 25 °C in Schneider's *Drosophila* medium supplemented with 10% (v/v) heat-inactivated fetal bovine serum, 100 U/ml penicillin, and 100 μg/ml streptomycin. Cells in 60 mm plates (1.5×10^6 cells/plate) were co-transfected with 950 ng pAc5.1-SCAT3 and 50 ng pAc5co-Hygro (Kondo et al., 1997; gift from Nagata S) using Effectene Transfection Reagent. Transfection was performed according to the manufacturer's protocol. After 48 h, cells were passaged into a 100 mm dish with 300 μg/ml Hygromycin B containing selective medium. The selective medium was replaced every 4-5 d. After 2 weeks, ECFP/Venus fluorescent-positive colonies were gently transferred into a 96-well plate with a pipette. Colonies with strong fluorescence were passaged into a 24-well plate. The established cell lines were cultured with selective medium during the following experimental procedures. Cells in four-compartment glass bottom dishes (Greiner, #627870; 2.0×10^5 cells/compartment) were cultured in 400 μl selective medium overnight. The medium was replaced 12 h before ROS treatment. Cells were then treated with MilliQ (MQ), 0.5 or 2.0 mM paraquat (PQ), or 0.5 or 2.0 mM H_2O_2 for 16 h. Images were taken with a Leica TCS SP8 confocal microscope (Leica Microsystems). For every experimental condition, images from six fields of views were taken.

Cell Fragmentation

VC3Ai$^+$ cell fragmentation patterns were divided into eight groups (0, 2, 3, 4, 5, 6, 7, 8) (Fig. S6E). Representative images are shown in Fig. S6D.

QUANTIFICATION AND STATISTICAL ANALYSIS

The groups were compared using a one-way analysis of variance (ANOVA) with Dunnett's test for Fig. 1D, 2B, 5H, 5K, 6G, and 6H, or with Sidak's multiple comparison test for Fig. S5B. For Fig. 6B, an unpaired two-tailed Student's t-test was performed. Analyses were conducted using GraphPad Prism 5 (GraphPad Software, Inc., CA, USA). All error bars in the figures represent standard errors (SE) of the mean. No statistical methods were used to set the sample size. Experiments were neither randomized nor analyzed blindly.

SUPPLEMENTAL REFERENCES

Chiba, M., Kamiya, M., Tsuda-Sakurai, K., Fujisawa, Y., Kosakamoto, H., Kojima, R., Miura, M., and Urano, Y. (2019). Activatable photosensitizer for targeted ablation of lacZ-positive cells with single-cell resolution. Acs. Central Sci. *5*, 1676-1681.

Dominguez, M., Wasserman, J.D., and Freeman, M. (1998). Multiple functions of the EGF receptor in *Drosophila* eye development. Curr. Biol. *8*, 1039–1048.

Hay, B.A., Wassarman, D.A., and Rubin, G.M. (1995). *Drosophila* homologs of baculovirus inhibitor of apoptosis proteins function to block cell death. Cell *83*, 1253-1262.

Kanuka, H., Kuranaga, E., Takemoto, K., Hiratou, T., Okano, H., and Miura, M. (2005). *Drosophila* caspase transduces Shaggy/GSK-3β kinase activity in neural precursor development. EMBO J. *24*, 3793-3806, 2005

Kondo, T., Yokokura, T., and Nagata, S. (1997). Activation of distinct caspase-like proteases by Fas and reaper in *Drosophila* cells. Proc. Natl. Acad. Sci. USA *94*, 11951-11956.

Koto, A., Kuranaga, E., and Miura, M. (2009). Temporal regulation of *Drosophila* IAP1 determines caspase functions in sensory organ development. J Cell Biol *187*, 219-231.

Koto, A., Kuranaga, E., and Miura, M. (2011). Apoptosis ensures spacing pattern formation of *Drosophila* sensory organs. Curr. Biol. *21*, 278-287.

Levayer, R., Dupont, C., and Moreno, E. (2016). Tissue Crowding Induces Caspase-

Dependent Competition for Space. Curr. Biol. *26*, 670-677.

Marinari, E., Mehonic, A., Curran, S., Gale, J., Duke, T., and Baum, B. (2012). Live-cell delamination counterbalances epithelial growth to limit tissue overcrowding. Nature *484*, 542-545.

Moreno, E., Valon, L., Levillayer, F., and Levayer, R. (2019). Competition for space induces cell elimination through compaction-driven ERK downregulation. Curr. Biol. *29*, 23-34 e8.

Obata, F., Kuranaga, E., Tomioka, K., Ming, M., Takeishi, A., Chen, C.H., Soga, T., and Miura, M. (2014). Necrosis-driven systemic immune response alters SAM metabolism through the FOXO-GNMT axis. Cell Rep *7*, 821-833.

Quinn, L.M., Dorstyn, L., Mills, K., Colussi, P.A., Chen, P., Coombe, M., Abrams, J., Kumar, S., and Richardson, H. (2000). An essential role for the caspase dronc in developmentally programmed cell death in *Drosophila*. J. Biol Chem 275, 40416-40424.

Schott, S., Ambrosini, A., Barbaste, A., Benassayag, C., Gracia, M., Proag, A., Rayer, M., Monier, B., and Suzanne, M. (2017). A fluorescent toolkit for spatiotemporal tracking of apoptotic cells in living *Drosophila* tissues. Development 144, 3840-3846.

Sekyrova, P., Bohmann, D., Jindra, M., Uhlirova M. (2010). Interaction between *Drosophila* bZIP proteins Atf3 and Jun prevents replacement of epithelial cells during metamorphosis. Development *137*, 141-150.

Shinoda, N., Hanawa, N., Chihara, T., Koto, A., and Miura, M. (2019). Dronc-independent basal executioner caspase activity sustains Drosophila imaginal tissue growth. Proc. Natl. Acad. Sci. USA *116*, 20539-20544.

Siegrist, S.E., Hague, N.S., Chen, C.H., Hay, B.A., and Hariharan, I.K. (2010). Inactivation of both foxo and reaper promotes long-term adult neurogenesis in *Drosophila*. Curr. Biol. *20*, 643-648.

Sykiotis, G.P., and Bohmann, D. (2008). Keap1/Nrf2 signaling regulates oxidative stress

tolerance and lifespan in *Drosophila*. Dev. Cell *14*, 76-85.

Takemoto, K., Nagai, T., Miyawaki, A., and Miura, M. (2003). Spatio-temporal activation of caspase revealed by indicator that is insensitive to environmental effects. J. Cell Biol. *160*, 235-243.

Tang, H.L., Tang, H.M., Fung, M.C., and Hardwick, J.M. (2015). In vivo CaspaseTracker biosensor system for detecting anastasis and non-apoptotic caspase activity. Sci. Rep. *5*, 9015.

Tsuneizumi, K., Nakayama, T., Kamoshida, Y., Kornberg, T. B., Christian, J. L., and Tabata, T. (1997). Daughters against dpp modulates dpp organizing activity in Drosophila wing development. Nature *389*, 627–631.